

# The Secular Evolution of the Primordial Kuiper Belt

Joseph M. Hahn

*Lunar and Planetary Institute, 3600 Bay Area Boulevard, Houston, TX 77058*

*email: hahn@lpi.usra.edu*

*phone: 281-486-2113*

*fax: 281-486-2162*

*Submitted to The Astrophysical Journal April 5, 2003*

*Revised May 26, 2003*

*Accepted May 29, 2003*

## ABSTRACT

A model that rapidly computes the secular evolution of a gravitating disk–planet system is developed. The disk is treated as a nested set of gravitating rings, with the rings’/planets’ time–evolution being governed by the classical Laplace–Lagrange solution for secular evolution but modified to account for the disk’s finite thickness  $h$ . The Lagrange planetary equations for this system yield a particular class of spiral wave solutions, usually denoted as apsidal density waves and nodal bending waves. There are two varieties of apsidal waves—long waves and short waves. Planets typically launch long density waves at the disk’s nearer edge or else at a secular resonance in the disk, and these waves ultimately reflect downstream at a more distant disk edge or else at a  $Q$ –barrier in the disk, whereupon they return as short density waves. Planets also launch nodal bending waves, and these have the interesting property that they can stall in the disk, that is, their group velocity plummets to zero upon approaching a region in the disk that is too thick to support the continued propagation of bending waves.

The rings model is used to compute the secular evolution of a Kuiper Belt having a variety of masses, and it is shown that the early massive Belt was

very susceptible to the propagation of low-amplitude apsidal and nodal waves launched by the giant planets. For instance, these waves typically excited orbits to  $e \sim \sin i \sim 0.01$  in a primordial Kuiper Belt of mass  $M_{KB} \sim 30$  Earth-masses. Although these orbital disturbances are quite small, the resulting fractional variations in the disk’s surface density due to the short density waves is usually large, typically of order unity. This epoch of apsidal and nodal wave propagation probably lasted throughout the Belt’s first  $\sim 10^7$  to  $\sim 5 \times 10^8$  years, with the waves being shut off between the time when the large  $R \gtrsim 100$  km KBOs first formed and when the Belt was subsequently eroded and stirred up to its present configuration.

## 1. Introduction

The Kuiper Belt is a vast swarm of comets orbiting at the Solar System’s outer edge. This Belt is comprised of debris that was left over from the epoch of planet formation, and this swarm’s distribution of orbit elements preserves a record of events that had occurred when the Solar System was still quite young. A common goal of nearly all dynamical studies of the Kuiper Belt is to decipher this Kuiper Belt record. However this record is still open to some interpretation.

The dots in Fig. 4 give the Kuiper Belt Objects (KBOs) eccentricities  $e$  and inclinations  $i$  versus their semimajor axes  $a$ . This Figure reveals the KBOs’ three major dynamical classes: the Plutinos which inhabit Neptune’s 3:2 resonance at  $a = 39.5$  AU, the Main Belt KBOs which are the non-resonant KBOs orbiting between  $40 \lesssim a \lesssim 48$  AU, and the more distant Scattered KBOs that live in eccentric, nearly Neptune-crossing orbits. The Figure also shows that the Plutinos and the Scattered KBOs have inclinations that span  $0 \lesssim i \lesssim 30^\circ$ , while the Main Belt KBOs appear to have a bimodal distribution of inclinations centered on  $i \simeq 2^\circ$  and  $i \simeq 17^\circ$  (Brown 2001). Note that accretion models show that these large  $\sim 100+$  km KBOs must have first formed from much smaller planetesimal seeds that were initially in nearly circular and coplanar orbits having  $e$  and  $\sin i \lesssim 0.001$  (Kenyon & Luu 1999). However gravitational self-stirring cannot account for the Kuiper Belt’s current excited state, so one or more mechanisms must also have stirred up the Kuiper Belt since the time of formation.

The orbits of the Scattered KBOs are perhaps the most easily understood. These objects likely have had one or more close encounters with Neptune which lofted these bodies into eccentric, inclined orbits (Duncan & Levison 1997). Repeated encounters with Neptune cause these objects’ semimajor axes and eccentricities to evolve stochastically along the Neptune-crossing curve shown in Fig. 4, and most of these bodies are ultimately ejected or accreted by

the giant planets. However Neptune has numerous weak, high-order mean motion resonances that thread the Kuiper Belt, and these resonances permit some of these Scattered objects to diffuse to lower eccentricities. This allows a small percentage of the Scattered objects to persist over the age of the Solar System at eccentricities just below the Neptune-crossing curve seen Fig. 4 (Duncan & Levison 1997). This diffusion to lower eccentricities may also have been more pronounced had Neptune’s orbit also migrated outwards. In particular, Gomes (2003) shows that during the epoch of planet migration, mean motion and secular resonances act as pathways that allow some scattered KBOs to descend *irreversibly* into lower-eccentricity orbits that are far from the Neptune-crossing curve and hence stable. Since Scattered KBOs have large inclinations of  $i \gtrsim 10^\circ$ , this process might also account for the Main Belt’s bimodal inclination distribution, with the  $i \sim 2^\circ$  component representing the Main Belt’s native population of low-inclination KBOs, and the  $i \sim 17^\circ$  being due to scattered invaders who were deposited in the Main Belt by Neptune. However this process is quite inefficient since only  $\varepsilon \sim 0.1\%$  of these Scattered KBOs manage to find orbits that are stable over a solar age (Gomes 2003).

The possibility that Neptune’s orbit had expanded outwards is also supported by the cluster of KBOs that inhabit Neptune’s 3:2 resonance (see Figure 4). This may have occurred when Neptune had first formed and began to vigorously scatter the local planetesimal debris. This process can drive an exchange of angular momentum between the planets and the planetesimal disk (Fernandez & Ip 1984), so this episode of disk-clearing can result in a rearrangement of all of the giant planets’ orbits over a timescale of  $\sim 10^7$  years (Hahn & Malhotra 1999). Outward planet migration will also cause Neptune’s mean-motion resonances to sweep out across the primordial Kuiper Belt, and these migrating resonances are quite effective at capturing KBOs and pumping up their eccentricities (Malhotra 1995). Models of this process show that if Neptune’s orbit had in fact smoothly expanded some  $\Delta a \sim 7$  AU over a timescale longer than a few million years, then resonance capture would have deposited numerous KBOs in the 3:2 and the 2:1 resonances with eccentricities distributed over  $0 \lesssim e \lesssim 0.3$  (Malhotra 1995; Chiang & Jordan 2002). Although numerous KBOs do indeed inhabit Neptune’s 3:2 resonance, only a handful are known to live near the 2:1 resonance at  $a = 47.8$  AU, and many of these bodies have eccentricities of  $e \sim 0.3$  which puts them quite near the Neptune-crossing curve (see Fig. 4). Thus it is possible that some or all of the bodies orbiting near  $a = 47.8$  AU might instead be members of the Scattered Belt. Thus if planet migration did indeed occur, then the apparent low abundance of KBOs at the 2:1 resonance is a mystery that can only be partly due to the observational bias that selects against the discovery of lower eccentricity objects at the 2:1 (Jewitt, Luu, & Trujillo 1998).

But of particular interest here is the Main Belt which preserves additional evidence for another mechanism having stirred up the Kuiper Belt. Again, if Neptune did indeed migrate

outwards  $\Delta a \sim 7$  AU, then the entire Main Belt was swept by the advancing 2:1 resonance. Models of planet migration show that the efficiency of resonance capture is no more than  $\sim 50\%$  (Chiang & Jordan 2002), so the current members of the Main Belt evidently avoided permanent capture by slipping through the advancing 2:1 resonance. However this planet migration scenario is utterly unable to account for the high inclinations of  $0 \lesssim i \lesssim 30^\circ$  observed in the Main Belt (see Fig. 4), since the N-body simulations show that the advancing 2:1 resonance typically excites Main Belt inclinations by only a few degrees (Malhotra 1995; Chiang & Jordan 2002). Evidently, an additional mechanism is also responsible for exciting the Main KBO Belt. It has been shown that sizable KBO excitation can occur if a recently-formed Neptune had been scattered outwards by Jupiter and/or Saturn into a Belt-crossing orbit (Thommes, Duncan, & Levison 2002). Another possible source of KBO excitation is the invasion of the Main Belt by the Scattered Belt (Gomes 2003). However this latter process is a very inefficient mechanism having  $\varepsilon \sim 0.001$ ; an alternate mechanism that is possibly more efficient will be explored below.

It has also been suggested that secular resonance sweeping may have been responsible for exciting the Kuiper Belt (Nagasawa & Ida 2000). Note that the locations of the secular resonances are very sensitive to the Solar System’s mass distribution. Consequently, the depletion of the solar nebula (which includes perhaps  $\sim 99\%$  of the Solar System’s initial mass content) could have driven these secular resonances across vast tracts of the Solar System. Indeed, the model by Nagasawa & Ida (2000) suggests that if the nebula was depleted on a timescale of  $\tau \sim 10^7$  years, Main Belt inclinations of  $i \sim 20^\circ$  can be excited due to the passage of the  $\nu_{15}$  secular resonance that sweeps outwards to infinity as the nebula is depleted<sup>1</sup>. However this model is rather idealized in that it treats the Kuiper Belt as massless, which is a concern since a primordial Kuiper Belt having some mass is also susceptible to the propagation of very long-wavelength spiral waves that can be launched at a secular resonance in the disk (Ward & Hahn 1998, 2003). This issue is worth further examination since wave-action can alter the magnitude of resonant excitation considerably (Hahn, Ward, & Rettig 1995; Ward & Hahn 1998). But even if there is no resonance in

---

<sup>1</sup>It should be noted that the resulting inclination excitation is also sensitive to the tilt between the nebula midplane and the invariable plane. For instance Nagasawa & Ida (2000) place the nebula midplane in the ecliptic, and this results in substantial excitation. But if the nebula midplane is instead placed in the invariable plane, which is tilted  $1.6^\circ$  from the ecliptic, then almost no excess excitation results (Hahn & Ward 2002). We also note that the nebula models of Nagasawa & Ida (2000) as well as Hahn & Ward (2002) both treat the gas disk as a rigid slab of gas. However a more realistic treatment would allow the nebula disk to flex and warp in response to the planets’ secular perturbations. It is suspected that this additional degree of freedom will substantially alter the secular resonance sweeping; indeed, it can be argued that the  $\nu_{15}$  never did sweep across the Kuiper Belt on account of this flexure (E. Chiang and W. Ward, 2002, private communication), so perhaps secular resonance sweeping of the Kuiper Belt is actually a moot issue.

the disk, planets orbiting interior to a particle disk can still launch these spiral waves at the disk’s inner edge (Ward & Hahn 1998). Preliminary results from a model of secular resonance sweeping also reveals that a Kuiper Belt having only a modest amount of mass is utterly awash in these waves once the nebula is depleted (Hahn & Ward 2002). However the purpose of the present study is to first characterize the properties of these waves in the simpler, post–nebula environment, and to explore their cosmogonic implications. Thus the following will consider a suite of models of the secular evolution of the outer Solar System for primordial Kuiper Belts having a variety of masses.

Accretion models tell us that the primordial Kuiper Belt must have had a mass of  $M_{\text{KB}} \sim 30 M_{\oplus}$  in the  $30 < a < 50$  AU interval in order for Pluto and its cohort of KBOs to have formed and survive over the age of the Solar System (Kenyon & Luu 1999). A similar Kuiper Belt mass is also needed to drive Neptune’s orbital migration of  $\Delta a \sim 7$  AU (Hahn & Malhotra 1999). However the current mass is  $M_{\text{KB}} \sim 0.2 M_{\oplus}$  (Jewitt, Luu, & Trujillo 1998), so the Kuiper Belt appears to have been eroded by a factor of  $\sim 150$ . This may be due to a dynamical erosion of the Belt by Neptune or possibly by other perturbers that may once have been roaming about the outer Solar System, as well as due to the collisional erosion that has since ground all of the smaller KBOs down to dust grains that are then removed from the Solar System by radiation forces (Kenyon & Luu 1999; Kenyon & Bromley 2001). The following will give results obtained from models of the secular evolution of the outer Solar System for Kuiper Belts having masses in the interval  $0 \leq M_{\text{KB}} \leq 30 M_{\oplus}$ .

Section 2 derives the so–called rings model that will be used to study the secular evolution of disk–planet systems; the reader uninterested in these details might skip ahead to Section 3 or 4. Since spiral density and bending waves appear prominently in the model results, their properties are examined in Section 3. Section 4 will describe the model’s application to the primordial Kuiper Belt, and a summary of results is then given in Section 5.

## 2. The Secular Evolution of Disk–Planet Systems

The following shall treat the disk as a collection of nested gravitating rings in orbit about the Sun. Their mutual perturbations will cause these rings’ to slowly flex and tilt over time, and this evolution is governed by the Lagrange planetary equations.

## 2.1. the rings model

Begin with the gravitational potential that a single perturbing ring of mass  $m'$  exerts at the point  $\mathbf{r}$  on another ring of mass  $m$ :

$$\Phi'(\mathbf{r}) = - \int \frac{G\rho'dV'}{\Delta} \quad (1)$$

where  $G$  is the gravitation constant,  $\rho'$  is the mass density of the differential volume element  $dV'$ ,  $\Delta$  is the separation between the perturbing mass element  $\rho'dV'$  at  $\mathbf{r}'$  and the field point  $\mathbf{r}$ , and the integration proceeds over the three dimensional extent of ring  $m'$ . In the following, primed quantities will refer to the perturbing ring  $m'$  and unprimed quantities will refer to the perturbed ring  $m$ . Each ring can be thought of as a swarm of numerous particles all having a common semimajor axis  $a$  and an identical mean orbital eccentricity  $e$ , inclination  $i$ , longitude of periapse  $\tilde{\omega}$ , and longitude of ascending node  $\Omega$ . It is also assumed that these particles have an isotropic dispersion velocity  $c$  that gives rise to the ring's finite radial as well as vertical half-thickness  $h \simeq c/n$ , where  $n$  is the ring's mean motion. It shall also be assumed that the density  $\rho'$  varies only in the azimuthal direction due to the keplerian motion of the ring's particles; in this case the density is  $\rho' = \lambda'/4h^2$  where

$$\lambda' = \frac{m'r'}{2\pi a^2 \sqrt{1-e'^2}} \quad (2)$$

is the ring's azimuthal mass per unit length (Murray & Dermott 1999). In cylindrical coordinates  $\mathbf{r}' = (\ell', \phi', z')$  and  $dV' = \ell' d\ell' d\phi' dz'$ . If the slight radial variations in equation (1)'s integrand are ignored (*i.e.*,  $\int \ell' d\ell' \simeq 2r'h'$ ), the potential becomes

$$\Phi'(\mathbf{r}) \simeq - \int_{-\pi}^{\pi} d\phi' \int_{z'_o-h'}^{z'_o+h'} dz' \frac{G\lambda'r'}{2h'\Delta}. \quad (3)$$

where  $z'_o(\phi')$  is the longitude-dependent height of the perturbing ring's midplane from the  $z = 0$  plane. Of course the perturbed ring  $m$  also has a radial and vertical half-thickness  $h$ , and it is useful to form an effective potential by averaging  $\Phi'(\mathbf{r})$  over the radial and vertical extent of ring  $m$ :

$$\langle \Phi'(\mathbf{r}) \rangle = \int_{-h}^h \frac{d\ell}{2h} \int_{z_o-h}^{z_o+h} \frac{dz}{2h} \Phi'(\mathbf{r}) \equiv - \int_{-\pi}^{\pi} d\phi' \frac{G\lambda'r'}{r} Q \quad (4)$$

where

$$Q \simeq \int_{z_o-h}^{z_o+h} \frac{dz}{2h} \int_{z'_o-h'}^{z'_o+h'} \frac{dz'}{2h'} \frac{r}{\Delta} \quad (5)$$

where again the slight variations in the integrand with  $\ell$  are ignored, and that only  $\Delta$  is assumed to be sensitive to the variations in  $z$  and  $z'$ . Note that this averaging of  $\Phi'$  is essential in order for the algorithm developed below to conserve angular momentum.

The next task is to evaluate the double integrals in  $Q$ . First note that the separation  $\Delta$  between the perturbing mass element  $\rho' dV'$  at  $\mathbf{r}'$  and the field point  $\mathbf{r}$  obeys  $\Delta^2 = r^2 + r'^2 - 2\sqrt{(r^2 - z^2)(r'^2 - z'^2)} \cos(\phi' - \phi) - 2zz'$  where  $r^2 = \ell^2 + z^2$ . Setting  $\alpha \equiv r'/r$ ,  $\beta \equiv z/r$ , and  $\beta' \equiv z'/r'$ , then

$$\left(\frac{\Delta}{r}\right)^2 \simeq 1 + \alpha^2 - 2\alpha \cos(\phi' - \phi) + (\beta^2 + \beta'^2)\alpha \cos(\phi' - \phi) - 2\alpha\beta\beta' \quad (6)$$

to second order in the  $\beta$ 's, which are of order the rings' inclinations and are assumed small. Inserting this into the expression for  $Q$  yields

$$Q = \frac{1}{4\mathfrak{h}\mathfrak{h}'} \int_{\beta_o - \mathfrak{h}}^{\beta_o + \mathfrak{h}} d\beta \int_{\beta'_o - \mathfrak{h}'}^{\beta'_o + \mathfrak{h}'} d\beta' \left[ 1 + \alpha^2 - 2\alpha \cos \Delta\phi + (\beta^2 + \beta'^2)\alpha \cos \Delta\phi - 2\alpha\beta\beta' \right]^{-1/2} \\ = \int_{\beta'_o - \mathfrak{h}'}^{\beta'_o + \mathfrak{h}'} \frac{\ln(\Upsilon) d\beta'}{4\mathfrak{h}\mathfrak{h}' \sqrt{\alpha \cos \Delta\phi}} \quad (7)$$

where  $\mathfrak{h} \equiv h/r \simeq h/a$  and  $\mathfrak{h}' \equiv h'/r' \simeq h'/a'$  are the fractional half-thicknesses of rings  $m$  and  $m'$ ,  $\beta_o \equiv z_o/r$  and  $\beta'_o \equiv z'_o/r'$  are the rings' midplane latitudes,  $\Delta\phi \equiv \phi' - \phi$ , and the right-hand side of equation (7) is the result of doing the integration in  $\beta$ , where

$$\Upsilon = \frac{\beta'\alpha - \beta_o\alpha \cos \Delta\phi - \mathfrak{h}\alpha \cos \Delta\phi - \sqrt{\alpha \cos \Delta\phi(\Gamma + \varepsilon)}}{\beta'\alpha - \beta_o\alpha \cos \Delta\phi + \mathfrak{h}\alpha \cos \Delta\phi - \sqrt{\alpha \cos \Delta\phi(\Gamma - \varepsilon)}} \quad (8)$$

with  $\Gamma = 1 + \alpha^2 - 2\alpha \cos \Delta\phi + (\beta_o^2 + \mathfrak{h}^2 + \beta'^2)\alpha \cos \Delta\phi - 2\alpha\beta'\beta_o$  and  $\varepsilon = 2\mathfrak{h}(\beta_o \cos \Delta\phi - \beta')\alpha$ . The  $\beta$ 's and the  $\mathfrak{h}$ 's are assumed small, so  $\varepsilon$  is second order in the small quantities and is negligible when compared to other terms. Thus

$$\Upsilon \simeq \frac{1 - [\beta'\alpha - \beta_o\alpha \cos \Delta\phi - \mathfrak{h}\alpha \cos \Delta\phi] / \sqrt{\alpha \cos \Delta\phi \Gamma}}{1 - [\beta'\alpha - \beta_o\alpha \cos \Delta\phi + \mathfrak{h}\alpha \cos \Delta\phi] / \sqrt{\alpha \cos \Delta\phi \Gamma}} \simeq 1 + 2\mathfrak{h} \sqrt{\frac{\alpha \cos \Delta\phi}{\Gamma}} \quad (9)$$

so  $\ln \Upsilon \simeq 2\mathfrak{h} \sqrt{\alpha \cos \Delta\phi / \Gamma}$ . This is inserted back into equation (7) and the remaining integral over  $\beta'$  is evaluated similarly, yielding  $Q \simeq \ln(\Lambda) / 2\mathfrak{h}' \sqrt{\alpha \cos \Delta\phi}$  where

$$\Lambda = \frac{1 - [\beta_o\alpha - \beta'_o\alpha \cos \Delta\phi - \mathfrak{h}'\alpha \cos \Delta\phi] / \sqrt{\alpha \cos \Delta\phi(\Psi + \mathcal{Z} + \xi)}}{1 - [\beta_o\alpha - \beta'_o\alpha \cos \Delta\phi + \mathfrak{h}'\alpha \cos \Delta\phi] / \sqrt{\alpha \cos \Delta\phi(\Psi + \mathcal{Z} - \xi)}} \simeq 1 + 2\mathfrak{h}' \sqrt{\frac{\alpha \cos \Delta\phi}{\Psi + \mathcal{Z}}} \quad (10)$$

with  $\Psi \equiv 1 + \alpha^2 - 2\alpha \cos \Delta\phi(1 - H^2) \simeq (1 + \alpha^2)(1 + H^2) - 2\alpha \cos \Delta\phi$ ,  $H^2 \equiv (\mathfrak{h}^2 + \mathfrak{h}'^2)/2$ ,  $\mathcal{Z} = (\beta_o^2 + \beta_o'^2)\alpha \cos \Delta\phi - 2\alpha\beta_o\beta_o'$  and  $\xi \equiv 2\mathfrak{h}'(\beta_o' \cos \Delta\phi - \beta_o)\alpha$  is another negligible term. Inserting  $\ln \Lambda \simeq 2\mathfrak{h}'\sqrt{\alpha \cos \Delta\phi/(\Psi + \mathcal{Z})}$  back into  $Q$  yields

$$Q \simeq \frac{1}{\sqrt{\Psi + \mathcal{Z}}} \simeq \Psi^{-1/2} - \frac{1}{2}\mathcal{Z}\Psi^{-3/2}. \quad (11)$$

A Fourier expansion of  $\Psi^{-s}$  will be useful, *i.e.*,  $\Psi^{-s} = \frac{1}{2} \sum_{m=-\infty}^{\infty} \tilde{b}_s^{(m)} \cos m(\phi' - \phi)$  where

$$\tilde{b}_s^{(m)}(\alpha, \mathfrak{h}, \mathfrak{h}') = \frac{2}{\pi} \int_0^\pi \frac{\cos(m\phi) d\phi}{\{(1 + \alpha^2)[1 + \frac{1}{2}(\mathfrak{h}^2 + \mathfrak{h}'^2) - 2\alpha \cos \phi]\}^s} \quad (12)$$

is the softened Laplace coefficient. The usual unsoftened form is  $b_s^{(m)}(\alpha) = \tilde{b}_s^{(m)}(\alpha, 0, 0)$ . These two coefficients are nearly equal when  $\alpha$  is far from unity, but the softened form is finite at  $\alpha = 1$  whereas the unsoftened form diverges. Writing  $Q$  in terms of softened Laplace coefficients thus gives

$$Q \simeq \frac{1}{2} \sum_{m=-\infty}^{\infty} \cos m(\phi' - \phi) \left\{ \tilde{b}_{1/2}^{(m)} - \left[ \frac{1}{2}(\beta_o^2 + \beta_o'^2)\alpha \cos \Delta\phi - \beta_o\beta_o'\alpha \right] \tilde{b}_{3/2}^{(m)} \right\}, \quad (13)$$

which is then inserted in equation (4) to get the perturbing ring's potential

$$\langle \Phi' \rangle = - \int_{-\pi}^{\pi} d\phi' \frac{G\lambda'r'}{2r} \sum_{m=-\infty}^{\infty} \cos m(\phi' - \phi) \left\{ \tilde{b}_{1/2}^{(m)} - \left[ \frac{1}{2}(\beta_o^2 + \beta_o'^2)\alpha \cos(\phi' - \phi) - \alpha\beta_o\beta_o' \right] \tilde{b}_{3/2}^{(m)} \right\}. \quad (14)$$

The final task of this Section is to write the rings' coordinates in terms of its orbit elements

$$r \simeq a(1 - e \cos \nu - \frac{1}{2}e^2 + \frac{1}{2}e^2 \cos 2\nu) \quad (15a)$$

$$\phi = \tilde{\omega} + \nu \simeq \tilde{\omega} + M + 2e \sin M \quad (15b)$$

$$\beta_o = \frac{z_o}{r} \simeq \sin i \sin(\phi - \Omega) \quad (15c)$$

where  $\nu$  is the true anomaly of a ring–element at  $\mathbf{r}$  and  $M = nt$  is the corresponding mean anomaly. Inserting equations (15) into the potential  $\langle \Phi' \rangle$ , expanding to second order in the  $e$ 's and  $i$ 's, doing the  $\phi'$  integration in equation (14), and time–averaging the resulting expression over the orbital period of ring  $m$  then yields the time–averaged potential  $\langle \bar{\Phi}' \rangle$  experienced by ring  $m$  due to ring  $m'$  assuming small eccentricities and inclinations:

$$\langle \bar{\Phi}' \rangle = - \frac{Gm'}{a} \left[ \frac{1}{2}\tilde{b}_{1/2}^{(0)} + \frac{1}{8}(e^2 + e'^2)f + \frac{1}{4}ee' \cos(\tilde{\omega}' - \tilde{\omega})g - \frac{1}{8}(i^2 + i'^2)\alpha\tilde{b}_{3/2}^{(1)} + \frac{1}{4}ii' \cos(\Omega' - \Omega)\alpha\tilde{b}_{3/2}^{(1)} \right] \quad (16)$$



where the  $f$  and  $g$  functions are

$$f(\alpha, \mathfrak{h}, \mathfrak{h}') = \left( 2\alpha \frac{\partial}{\partial \alpha} + \alpha^2 \frac{\partial^2}{\partial \alpha^2} \right) b_{1/2}^{(0)} = \alpha \tilde{b}_{3/2}^{(1)} - 3\alpha^2 H^2 (2 + H^2) \tilde{b}_{5/2}^{(0)} \quad (17a)$$

$$g(\alpha, \mathfrak{h}, \mathfrak{h}') = \left( 2 - 2\alpha \frac{\partial}{\partial \alpha} - \alpha^2 \frac{\partial^2}{\partial \alpha^2} \right) b_{1/2}^{(1)} = -\alpha \tilde{b}_{3/2}^{(2)} + 3\alpha^2 H^2 (2 + H^2) \tilde{b}_{5/2}^{(1)} \quad (17b)$$

where  $H^2 = \frac{1}{2}(\mathfrak{h}^2 + \mathfrak{h}'^2)$  and  $\alpha$  has been redefined as  $\alpha = a'/a$ . The right-hand side of equations (17) are derived in Appendix A, and it is shown in Appendix B that the softened Laplace coefficients can be written in terms of complete elliptic integrals. Consequently, functions  $f$ ,  $g$ , and  $\tilde{b}_s^{(m)}$  all can be rapidly evaluated without relying upon a numerical integration of equation (12). It is also noted that the  $\tilde{b}_s^{(m)}$ ,  $f$ , and  $g$  functions obey the following reciprocal relations

$$\tilde{b}_s^{(m)}(\alpha^{-1}, \mathfrak{h}', \mathfrak{h}) = \alpha^{2s} \tilde{b}_s^{(m)}(\alpha, \mathfrak{h}, \mathfrak{h}') \quad (18a)$$

$$f(\alpha^{-1}, \mathfrak{h}', \mathfrak{h}) = \alpha f(\alpha, \mathfrak{h}, \mathfrak{h}') \quad (18b)$$

$$g(\alpha^{-1}, \mathfrak{h}', \mathfrak{h}) = \alpha g(\alpha, \mathfrak{h}, \mathfrak{h}'). \quad (18c)$$

These relations will be used in Section 2.2.1 to show that the equations of motion developed below conserve angular momentum.

The laborious procedure of expanding, integrating, and then time-averaging  $\langle \Phi' \rangle$  is not included here since a similar analysis can be found in Murray & Dermott (1999)<sup>2</sup>. Since the terms proportional to  $e'^2$  and  $i'^2$  as well as the first term in equation (16) do not contribute to the resulting dynamical equations, they may be neglected. The disturbing function  $R$  for ring  $m$  due to another ring  $m'$  is  $-1 \times$  the surviving terms in  $\langle \bar{\Phi}' \rangle$ , *i.e.*,

$$R = \frac{Gm'}{a} \left[ \frac{1}{8} f e^2 + \frac{1}{4} g e e' \cos(\tilde{\omega}' - \tilde{\omega}) - \frac{1}{8} \alpha \tilde{b}_{3/2}^{(1)} i'^2 + \frac{1}{4} \alpha \tilde{b}_{3/2}^{(1)} i i' \cos(\Omega' - \Omega) \right]. \quad (19)$$

Note that when  $\mathfrak{h} = \mathfrak{h}' = 0$  the disturbing function for a point mass  $m$  perturbed by point mass  $m'$  is recovered (Brouwer & Clemence 1961; Murray & Dermott 1999), which is to be expected since both a point mass as well as a thin ring have the same disturbing function to this degree of accuracy (Murray & Dermott 1999).

It should also be noted that many celestial mechanics texts develop two distinct expressions for the disturbing function  $R$ , one due to a perturber in an interior orbit having  $a' < a$ ,

---

<sup>2</sup>Actually Murray & Dermott (1999) derive the time-averaged acceleration (rather than a potential) that ring  $m'$  exerts on  $m$ , which they insert into the Gauss equations to obtain a set of dynamical equations equivalent to that obtained here when  $\mathfrak{h} = 0$ .

and another expression due to an exterior perturber having  $a' > a$  [c.f., Brouwer & Clemence (1961); Murray & Dermott (1999)]. However this pairwise development is unnecessary in this application since equation (19) is valid for  $\alpha = a'/a < 1$  as well as for  $\alpha > 1$ . Indeed, it is straightforward to show that these pairs of disturbing functions, such as equations (7.6) and (7.7) in Murray & Dermott (1999), are in fact equivalent to equation (19) with  $\mathbf{h} = \mathbf{h}' = 0$ ; they only appear distinct since one is a function of  $\alpha$  and the other is actually a function of  $\alpha^{-1}$ .

In terms of the variables

$$h = e \sin \tilde{\omega} \qquad p = i \sin \Omega \qquad (20a)$$

$$k = e \cos \tilde{\omega} \qquad q = i \cos \Omega, \qquad (20b)$$

the disturbing function can then be written

$$R = n^2 a^2 \left( \frac{m'}{M_\odot + m} \right) \left[ \frac{1}{8} f(h^2 + k^2) + \frac{1}{4} g(hh' + kk') - \frac{1}{8} \alpha \tilde{b}_{3/2}^{(1)}(p^2 + q^2) + \frac{1}{4} \alpha \tilde{b}_{3/2}^{(1)}(pp' + qq') \right] \qquad (21)$$

where the mean motion  $n = \sqrt{G(M_\odot + m)/a^3}$  with  $M_\odot$  being the solar mass.

### 2.1.1. the $N$ ring problem

For the more general problem of  $N$  perturbing rings, replace the perturbing ring mass  $m'$  with  $m_k$  and give all the other primed quantities the subscript  $k$ . The disturbing function  $R \rightarrow R_j$  for the perturbed ring having a mass  $m \rightarrow m_j$  is sum of equation (21) over all the other rings  $k \neq j$ . Setting  $\alpha_{jk} \equiv a_k/a_j$ ,  $n_j = \sqrt{G(M_\odot + m_j)/a_j^3}$ , and

$$A_{jj} = \frac{n_j}{4} \sum_{k \neq j} \left( \frac{m_k}{M_\odot + m_j} \right) f(\alpha_{jk}, \mathbf{h}_j, \mathbf{h}_k) \qquad (22a)$$

$$A_{jk} = \frac{n_j}{4} \left( \frac{m_k}{M_\odot + m_j} \right) g(\alpha_{jk}, \mathbf{h}_j, \mathbf{h}_k) \qquad j \neq k \qquad (22b)$$

$$B_{jj} = -\frac{n_j}{4} \sum_{k \neq j} \left( \frac{m_k}{M_\odot + m_j} \right) \alpha_{jk} \tilde{b}_{3/2}^{(1)}(\alpha_{jk}, \mathbf{h}_j, \mathbf{h}_k) \qquad (22c)$$

$$B_{jk} = \frac{n_j}{4} \left( \frac{m_k}{M_\odot + m_j} \right) \alpha_{jk} \tilde{b}_{3/2}^{(1)}(\alpha_{jk}, \mathbf{h}_j, \mathbf{h}_k) \qquad j \neq k, \qquad (22d)$$

that sum becomes

$$R_j = n_j a_j^2 \left[ \frac{1}{2} A_{jj} (h_j^2 + k_j^2) + \sum_{k \neq j} A_{jk} (h_j h_k + k_j k_k) + \frac{1}{2} B_{jj} (p_j^2 + q_j^2) + \sum_{k \neq j} B_{jk} (p_j p_k + q_j q_k) \right] \quad (23)$$

in the notation of Murray & Dermott (1999). The  $A_{jk}$  and the  $B_{jk}$  can be regarded as two  $N \times N$  matrices  $\mathbf{A}$  and  $\mathbf{B}$  whose entries describe the magnitude of the mutual gravitational interactions that are exerted among the  $N$  rings. In the following, quantities having a  $j$  subscript will always refer to the perturbed ring in question while the  $k$  subscript will always refer to another perturbing ring.

The time-variation of the rings' orbit elements is given by the Lagrange planetary equations; to lowest order in the  $e$ 's and  $i$ 's these are (Brouwer & Clemence 1961; Murray & Dermott 1999)

$$\frac{dh_j}{dt} \simeq \frac{\partial R_j / \partial k_j}{n_j a_j^2} = \sum_{k=1}^N A_{jk} k_k \quad (24a)$$

$$\frac{dk_j}{dt} \simeq - \frac{\partial R_j / \partial h_j}{n_j a_j^2} = - \sum_{k=1}^N A_{jk} h_k \quad (24b)$$

$$\frac{dp_j}{dt} \simeq \frac{\partial R_j / \partial q_j}{n_j a_j^2} = \sum_{k=1}^N B_{jk} q_k \quad (24c)$$

$$\frac{dq_j}{dt} \simeq - \frac{\partial R_j / \partial p_j}{n_j a_j^2} = - \sum_{k=1}^N B_{jk} p_k, \quad (24d)$$

and their well-known Laplace-Lagrange solution is

$$h_j(t) = \sum_{i=1}^N E_{ji} \sin(g_i t + \beta_i) \quad (25a)$$

$$k_j(t) = \sum_{i=1}^N E_{ji} \cos(g_i t + \beta_i) \quad (25b)$$

$$p_j(t) = \sum_{i=1}^N I_{ji} \sin(f_i t + \gamma_i) \quad (25c)$$

$$q_j(t) = \sum_{i=1}^N I_{ji} \cos(f_i t + \gamma_i) \quad (25d)$$

where  $g_i$  is the  $i^{\text{th}}$  eigenvalue of the  $\mathbf{A}$  matrix,  $f_i$  is the  $i^{\text{th}}$  eigenvalue of  $\mathbf{B}$ ,  $E_{ji}$  is the  $N \times N$  matrix formed from the  $N$  eigenvectors to  $\mathbf{A}$  and  $I_{ji}$  is the matrix of eigenvectors to  $\mathbf{B}$ , and  $\beta_i$  and  $\gamma_i$  are integration constants.

To apply this rings model, first assign to the  $N$  rings their masses  $m_j$ , their semimajor axes  $a_j$ , and their fractional half-thickness  $\mathfrak{h}_j$ . Planets are represented as thin rings having  $\mathfrak{h}_j = 0$ . Then construct the system’s  $\mathbf{A}$  and  $\mathbf{B}$  matrices and compute their eigenvalues  $g_i$ ,  $f_i$  and the eigenvector arrays  $E_{ji}$  and  $I_{ji}$ . The rings’ initial orbits  $e_j(0)$ ,  $i_j(0)$ ,  $\tilde{\omega}_j(0)$ , and  $\Omega_j(0)$  are then used to determine the integration constants  $\beta_i$  and  $\gamma_i$  as well as to rescale the eigenvectors  $E_{ji}$  and  $I_{ji}$  such that equations (25) agree with the initial conditions. A handy recipe for this particular task is given in Murray & Dermott (1999). Equations (25) are then used to compute the system’s time-history, and orbit elements are recovered via  $e_j^2 = h_j^2 + k_j^2$ ,  $i_j^2 = p_j^2 + q_j^2$ ,  $\tan \tilde{\omega}_j = h_j/k_j$ , and  $\tan \Omega_j = p_j/q_j$ .

The rather laborious derivation given above thus confirms the assertion by Tremaine (2001) that one only needs to soften the Laplace coefficients in order to use the Laplace–Lagrange solution for calculating the secular evolution of a continuous disk. However Section 2.2.1 will show that this softening must be done judiciously such that equation (18a) is obeyed in order for the solution to preserve the system’s angular momentum.

## 2.2. tests of the rings model

Several tests have been devised in order to demonstrate that the rings model described above behaves as expected.

### 2.2.1. angular momentum conservation

The equations developed above conserve the system’s total  $z$ -component of angular momentum  $L_z = \sum_j m_j n_j a_j^2 \sqrt{1 - e_j^2} \cos(i_j)$ . To show this, expand  $L_z$  to second order in the  $e$ ’s and  $i$ ’s, which is the same degree of precision to which the disk potential is developed above. This gives  $L_z \simeq L_0 - L_e - L_i$  where

$$L_e = \frac{1}{2} \sum_j m_j n_j a_j^2 e_j^2 \tag{26a}$$

$$L_i = \frac{1}{2} \sum_j m_j n_j a_j^2 i_j^2 \tag{26b}$$

and  $L_0 = \sum_j m_j n_j a_j^2$  is a constant. It is shown in Appendix C that the dynamical equations (24) conserve angular momenta to second order in the  $e$ ’s and  $i$ ’s, that is,  $dL_e/dt = 0$  and  $dL_i/dt = 0$ . When the rings model is used to calculate the secular evolution of a ‘sparse’ system, such as the Jupiter–Saturn system described below or one composed of all four giant

planets, the angular momenta  $L_e$  and  $L_i$  are preserved to near machine limits to a fractional precision of  $\sim 10^{-7}$  in this single floating-point implementation. This is true regardless of whether the planets are represented as thin rings having  $\mathfrak{h}_j = 0$  or as thick rings with  $\mathfrak{h}_j > 0$ . However  $L_z$  conservation is a little worse,  $\sim 10^{-6}$ , in the ‘crowded’ systems described in Section 4 that consist of a few planets plus a disk comprised of many closely-packed rings. However these errors are always smaller, by a factor of  $\sim 10^4$  to  $10^5$ , than the angular momenta associated with the disturbances and waves seen in these disks. Thus the wave-like disk behavior reported below is real and is not due to a diffusion of some numerical error.

### 2.2.2. *Jupiter and Saturn*

Murray & Dermott (1999) use the Laplace–Lagrange planetary solution, equations (25), to study a system composed of Jupiter and Saturn. The rings model developed here reproduces that system’s  $\mathbf{A}$  and  $\mathbf{B}$  matrices, eigenvector arrays  $E_{ji}$  and  $I_{ji}$ , eigenvalues  $g_i$  and  $f_i$ , and integration constants  $\beta_i$  and  $\gamma_i$ , to the same precision quoted by Murray & Dermott (1999), provided one sets  $n_j = \sqrt{GM_\odot/a_j^3}$  and  $\mathfrak{h}_j = 0$ . The rings model also reproduces the figures in Murray & Dermott (1999) that show this system’s orbital history, as well as the figures showing the forced orbit elements of numerous other massless ‘test-rings’ orbiting throughout this system. However it should be noted that rigorous angular momentum conservation actually requires setting  $n_j = \sqrt{G(M_\odot + m_j)/a_j^3}$  instead.

### 2.2.3. *precession in an axisymmetric disk*

Heppenheimer (1980) points out that a massless test particle orbiting in a smooth, axisymmetric disk experiences a *regression* of its longitude of periapse, *i.e.*,  $\dot{\tilde{\omega}} < 0$ , which is the opposite of the usual prograde apse precession that occurs throughout the Solar System. As Ward (1981) shows, it is the nearby disk parcels whose orbits actually cross the test particle’s orbit that drives periapse regression at a rate that exceeds the prograde contribution from the more distant parts of the disk.

The rings code also reproduces this phenomenon. An annulus having a surface density  $\sigma'$ , mass  $\delta m' = 2\pi\sigma' a' da'$ , a semimajor axis  $a'$ , and a fractional half-thickness  $\mathfrak{h}'$  contributes  $\delta R = n^2 a^2 [f(\alpha, 0, \mathfrak{h}') e^2 - \alpha \tilde{b}_{3/2}^{(1)}(\alpha, 0, \mathfrak{h}') i^2] \delta m' / 8M_\odot$  to the particle’s disturbing function [see equation (19) with  $e' = i' = 0$ ]. Adopting a power-law in the disk surface density,  $\sigma' = \sigma(a)\alpha^{-r}$  where  $\alpha = a'/a$ , the total disturbing function integrated across a semi-infinite disk

is

$$R = \int \delta R = \frac{1}{2} \mu_d n^2 a^2 [I_{\tilde{\omega}} e^2 - I_{\Omega} i^2] \quad (27)$$

where  $\mu_d = \pi \sigma(a) a^2 / M_{\odot} = \pi G \sigma / a n^2$  is the so-called normalized disk mass and

$$I_{\tilde{\omega}} = \frac{1}{2} \int_0^{\infty} \alpha^{1-r} f(\alpha, 0, \mathfrak{h}') d\alpha \quad (28a)$$

$$I_{\Omega} = \frac{1}{2} \int_0^{\infty} \alpha^{2-r} \tilde{b}_{3/2}^{(1)}(\alpha, 0, \mathfrak{h}') d\alpha. \quad (28b)$$

Note that  $I_{\tilde{\omega}}$  and  $I_{\Omega}$  are double integrals according to the definitions of  $\tilde{b}_s^{(m)}$  and  $f$ , equations (12) and (17a). However these integrals are analytic for selected power laws  $r$ . For instance, setting  $r = 1$  or  $r = 2$  and then instructing symbolic math software such as MAPLE to do the radial integration first and the angular integration second yields  $I_{\tilde{\omega}} = -1/\sqrt{1 + \mathfrak{h}'^2/2} \simeq -1$  and  $I_{\Omega} = [\mathfrak{h}'^{-1} + \sqrt{1 + \mathfrak{h}'^2/4} + \mathfrak{h}'/2]/\sqrt{(1 + \mathfrak{h}'^2/4)(1 + \mathfrak{h}'^2/2)} \simeq 1/\mathfrak{h}'$  for small  $\mathfrak{h}'$ . The Lagrange planetary equations then give the test-ring's precession rates:

$$\dot{\tilde{\omega}} \simeq \frac{\partial R / \partial e}{n a^2 e} = I_{\tilde{\omega}} \mu_d n \simeq -\mu_d n \quad (29a)$$

$$\dot{\Omega} \simeq \frac{\partial R / \partial i}{n a^2 i} = -I_{\Omega} \mu_d n \simeq -\mu_d n / \mathfrak{h}'. \quad (29b)$$

Very similar precession rates were previously derived in Heppenheimer (1980) and Ward (1981). Note that the model rings start to overlap when their fractional radial thickness  $2\mathfrak{h}'$  exceeds the rings' fractional separation  $\delta = \Delta a / a$ , so a massless test ring should precess at the above rates when the disk-rings are sufficiently overlapping.

These expectations are tested by constructing a  $50 M_{\oplus}$  disk having an  $r = 2$  power-law surface density using 200 circular, coplanar rings arranged over  $10 < a < 100$  AU, with a number of thin, massless ‘test-rings’ also orbiting within this disk. Several simulations are performed with the massive rings having a variety of thicknesses  $\mathfrak{h}'$ . As expected, those test-rings that reside far from the disk’s edges precess at rates given by equation (29) whenever the disk-rings are sufficiently overlapping, namely, when  $\mathfrak{h}' \geq 2\delta$ .

#### 2.2.4. precession in an eccentric disk

Although a particle’s periapse will experience retrograde precession when embedded in an axisymmetric disk, prograde precession is possible in a non-axisymmetric disk. For instance, prograde precession is evident in the N-body simulations of an eccentric stellar disk orbiting the putative black hole at the center of the Andromeda galaxy M31 (Jacobs and

Sellwood 2001). These simulated disks have masses  $\sim 0.1$  times the central mass, with the interior parts of the disk being progressively more eccentric. These simulations reveal a long-lived overdense region in the direction of apoapse that persists due to a coherent alignment of the particles’ periapse, with the density pattern rotating in a prograde sense at rates that increase with the disk mass. It should be noted that the disk particles’ eccentricities are not always small, so these N–body simulations cannot be used as a quantitative benchmark for the rings code. Nonetheless, it is comforting to find that the rings code does indeed reproduce the density patterns seen in the N–body disks that precess at rates very similar to that reported in Jacobs and Sellwood (2001).

### 3. Spiral Wave Theory

Section 4 will use the preceding rings model to demonstrate that apsidal density waves and nodal bending waves may have once propagated throughout the Kuiper Belt. An apsidal wave is a one–armed spiral density wave that slowly rotates over a periapse precession timescale. Similarly, a nodal wave is a one–armed spiral bending wave that rotates over a nodal precession timescale.

A brief review of spiral wave theory is in order. Many of the waves’ properties, such as their wavelength and propagation speed, are readily extracted from the waves’ dispersion relations. These dispersion relations are usually obtained from solutions to the Poisson and Euler equations for the disk. However the following will show that these dispersion relations may also be derived from the Lagrange planetary equations.

#### 3.1. Apsidal Density Waves

The disturbing function  $R(a)$  for the disk material orbiting at a semimajor axis  $a$  is obtained from equation (19) with the perturbing mass  $m'$  replaced by the differential mass  $dm'$  whose contributions are integrated across a semi–infinite disk:

$$R(a) = \frac{1}{2}\mu_d n^2 a^2 \int_0^\infty \alpha^{1-r} \left[ \frac{1}{2}e^2 f(\alpha, \mathfrak{h}, \mathfrak{h}) + ee' \cos(\tilde{\omega}' - \tilde{\omega})g(\alpha, \mathfrak{h}, \mathfrak{h}) \right] d\alpha. \quad (30)$$

where  $e'(\alpha)$  and  $\tilde{\omega}'(\alpha)$  are the orbit elements of the perturbing parts of the disk, the unprimed quantities refer to the perturbed annulus at  $a$ ,  $r$  is the power–law for the disk’s surface density variation, and a constant fractional thickness  $\mathfrak{h}$  is assumed throughout the disk. The

Lagrange planetary equations then give the disk’s periapse precession rate at  $a$ :

$$\dot{\tilde{\omega}}(a) \simeq \frac{\partial R/\partial e}{na^2e} = \mu_d n (I_{\tilde{\omega}} + I_{dw}) \quad (31)$$

where  $I_{\tilde{\omega}} \simeq -1$  is from the left term in equation (30) and is the contribution by an undisturbed disk to its own precession [see equations (28–29)], and the right term is

$$I_{dw} = \frac{1}{2} \int_0^\infty \frac{e'}{e} \cos(\tilde{\omega}' - \tilde{\omega}) \alpha^{1-r} g(\alpha, \mathfrak{h}, \mathfrak{h}) d\alpha, \quad (32)$$

which is the relative rate at which the density wave drives its own precession.

It is expected that the eccentricities associated with a spiral density wave will vary only slowly with distance  $a$  such that  $e'(\alpha)/e \simeq 1$ . The spiral wave will also organize the disk’s longitude of periapse  $\tilde{\omega}$  such that it varies as  $\tilde{\omega}(a, t) = \dot{\tilde{\omega}}t - \int^a k(A) dA$ , where  $k(a)$  is the wavenumber and  $\lambda = 2\pi/|k|$  is the radial wavelength. If the spiral wave pattern is tightly wound such that  $\lambda \ll a$  and  $|ka| \gg 1$ , then the dominant contributions to  $I_{dw}$  are largely due to the nearby parts of the disk where  $\alpha = a'/a \sim 1 \pm \lambda/a$  and  $\tilde{\omega}' - \tilde{\omega} = -\int_a^{a'} k(A) dA \simeq -k(a' - a)$ , while the contributions from the more distant parts of the disk tend to cancel owing to the rapid oscillation of the cosine factor. Thus we can set  $\alpha = 1$  in equation (32) except where it appears as the combination  $x = \alpha - 1$  where  $|x| \ll 1$ . In this case the softened Laplace coefficients that are present in the  $g$  function can be replaced with the approximate forms that are valid for  $|x| \ll 1$  [see equation (B5)], so  $g$  becomes

$$g(x) \simeq \frac{2}{\pi} \frac{2\mathfrak{h}^2 - x^2}{(2\mathfrak{h}^2 + x^2)^2}. \quad (33)$$

It is also permitted to extend the lower integration limit in equation (32) to  $-\infty$  in the tight-winding limit, so

$$I_{dw} \simeq \frac{1}{2} \int_{-\infty}^\infty \cos(|ka|x) g(x) dx = |ka| e^{-\sqrt{2}\mathfrak{h}|ka|}. \quad (34)$$

And finally, if the wave is to remain coherent across this disk, this self-precession must occur at the same constant rate  $\omega$  throughout the disk, so  $\dot{\tilde{\omega}}(a) = \omega \simeq \mu_d (|ka| e^{-\sqrt{2}\mathfrak{h}|ka|} - 1)n$ . Note that this disturbing frequency  $\omega$ , which is also called the pattern speed, can also be identified as any one of the eigenfrequencies  $g_i$  that appear in equations (25). Usually it is another perturber that is responsible for launching the wave and causing the disk to precess in concert at the rate  $\omega$ , and this is usually at a rate that dominates over the non-wave contribution to the disk’s precession, *i.e.*,  $|\omega| \gg \mu_d n$ . This then yields the dispersion relation for tightly-wound apsidal density waves:

$$\omega \simeq e^{-\sqrt{2}\mathfrak{h}|ka|} \mu_d |ka| n \quad (35)$$



which has the dimensionless form

$$\omega_e(K) = Ke^{-K} \quad (36)$$

where  $\omega_e = \sqrt{2}\mathfrak{h}\omega/\mu_d n$  is the dimensionless frequency and  $K = \sqrt{2}\mathfrak{h}|ka|$  the dimensionless wavelength; Figure 1 plots  $\omega_e$  versus  $K$ . A more general dispersion relation for an  $m$ -armed spiral wave in a stellar disk is given in Toomre (1969), and in the limit that  $|\omega| \ll n$  the resulting formula with  $m = 1$  behaves qualitatively quite similar<sup>3</sup> to equation (36). Note that equation (35) also recovers the usual dispersion relation  $\omega = \mu_d|ka|n$  for apsidal waves in an infinitesimally thin disk when  $\mathfrak{h} = 0$ .

Note that  $\omega_e(K) > 0$  and that it also has a maximum at  $K = 1$  where  $\omega_e(1) = \exp(-1)$ . Since  $\omega_e$  is a function of semimajor axis  $a$ , the restriction  $0 < \omega_e(a) \lesssim 0.368$  indicates that apsidal waves can only propagate in a restricted interval in  $a$ . This restriction can also be viewed as a constraint on the disk thickness, namely,

$$\mathfrak{h} \lesssim 0.260\mu_d|n/\omega| \equiv \mathfrak{h}_Q. \quad (37)$$

Alternatively, equation (37) can also be viewed as an upper limit on the frequency  $\omega$  or a lower limit on the disk mass  $\mu_d$  wherein wave-action is permitted.

Waves having a wavenumber  $K < 1$  are called long waves since they have a wavenumber  $|k_L| \simeq (\omega/n)/\mu_d a$  and the longer wavelength  $\lambda_L = 2\pi/|k_L| \simeq 2\pi\mu_d(n/\omega)a$ , while short waves have wavenumbers  $K > 1$  or  $|k_S| > 1/\sqrt{2}\mathfrak{h}a$  and the shorter wavelength  $\lambda_S = 2\pi/|k_S| < 2\sqrt{2}\pi\mathfrak{h}a$ . These long and short density waves also correspond to the  $g$  and  $p$  modes, respectively, of Tremaine (2001). Writing  $\lambda_L$  in term of  $\mathfrak{h}_Q$  and then requiring  $\mathfrak{h} < \mathfrak{h}_Q$  also means that apsidal wave can propagate wherever  $\lambda_L \gtrsim 24h$ .

The rate at which apsidal waves propagate across the disk is given by their group velocity

$$c_g = \frac{d\omega}{dk} = s_k\mu_d(1 - K)e^{-K}na \quad (38)$$

where  $s_k = \text{sgn}(k)$ . Waves with  $s_k = +1$  are called trailing waves, and their longitude of perihelia  $\tilde{\omega}$  decreases with increasing semimajor axis  $a$ , while  $s_k = -1$  are leading waves whose longitude increases with  $a$ . Since the waves' group velocity  $c_g$  is proportional to the slope of the  $\omega_e(K)$  curve, the site where  $K = 1$  is a turning point where wave reflection occurs; in galactic dynamics this reflection site is known as a  $Q$  barrier. A long wave that approaches the  $Q$  barrier from the  $K < 1$  side of Figure 1 thus reflects as a short wave as it

---

<sup>3</sup>In this limit, Toomre's dispersion relation becomes  $\omega_T(K) = K\mathcal{F}$  where the reduction factor  $\mathcal{F}$  is a more complicated function of  $K$ . However a numerical evaluation of this function shows that  $\omega_T(K)$  has the same form as the  $\omega_e(K)$  curve shown in Figure 1.

continues along the  $K > 1$  side of the curve. The simulations shown in Section 4 also show that long trailing waves that instead strike a disk edge also reflect as short trailing waves.

### 3.2. surface density variations

The compression or rarefaction among the disk’s rings, or streamlines, is  $(\partial r/\partial a)^{-1}$ , which is also be the relative change in the disk’s surface density  $\sigma/\sigma_o$  associated with a density wave [c.f., Borderies, Goldreich & Tremaine (1985)]. For a small amount of compression,  $\sigma/\sigma_o = 1 + \Delta\sigma/\sigma_o$  where the fractional surface density variation is

$$\frac{\Delta\sigma}{\sigma_o} = \left(\frac{\partial r}{\partial a}\right)^{-1} - 1 \simeq \frac{\partial(ea)}{\partial a} \cos(\phi - \tilde{\omega}) + ea \frac{\partial\tilde{\omega}}{\partial a} \sin(\phi - \tilde{\omega}) \quad (39)$$

to lowest order in  $e$ . The second term dominates over the first in the tight-winding limit so  $|\Delta\sigma/\sigma_o| \sim \mathcal{O}(e|ka|)$ . Density waves are nonlinear when  $|\Delta\sigma/\sigma_o| > 1$ , and these large density variations are a consequence of overlapping streamlines. For long density waves having a wavenumber  $|k_L| = \omega/\mu_d a n$ , the disk’s streamlines will cross when the waves’ eccentricities exceed  $e_L \sim \mu_d \omega/n$ , while streamline crossing occurs among short waves when eccentricities exceed  $e_S \sim \sqrt{2}\mathfrak{h}$ . As the simulations of Section 4 will show, a dynamically cool Kuiper Belt is very susceptible to the propagation of short nonlinear density waves that facilitate streamline crossing. Depending upon the relative velocities of these crossed streamlines, apsidal wave-action might encourage accretion or else enhance collisional erosion among KBOs.

### 3.3. Nodal Bending Waves

The derivation of the dispersion relation for nodal bending waves, and its analysis, proceeds similarly. The disk’s integrated disturbing function is

$$R(a) = -\frac{1}{2}\mu_d n^2 a^2 \int_0^\infty \alpha^{2-r} \tilde{b}_{3/2}^{(1)}(\alpha, \mathfrak{h}, \mathfrak{h}) \left[ \frac{1}{2}i^2 - ii' \cos(\Omega' - \Omega) \right] d\alpha. \quad (40)$$

so the Lagrange planetary equation gives

$$\dot{\Omega}(a) \simeq \frac{\partial R/\partial i}{na^2 i} = \mu_d n (I_{bw} - I_\Omega) \quad (41)$$

where  $\Omega(a, t) = \dot{\Omega}t - \int^a k(A)dA$  and

$$I_{bw} = \frac{1}{2} \int_0^\infty \alpha^{2-r} \tilde{b}_{3/2}^{(1)}(\alpha, \mathfrak{h}, \mathfrak{h}) \cos[ka(\alpha - 1)] d\alpha \simeq \frac{e^{-\sqrt{2}\mathfrak{h}|ka|}}{\sqrt{2}\mathfrak{h}} \quad (42)$$

is the bending wave’s contribution to its own precession. The contribution from the undisturbed disk is  $I_\Omega \simeq 1/\sqrt{2\mathfrak{h}}$ , with the additional  $\sqrt{2}$  factor the result of changing the middle argument in equation (28b) from 0 to  $\mathfrak{h}$ . Since  $\omega = \dot{\Omega}$  is a constant for a coherent wave, the dispersion relation for tightly-wound nodal bending waves is

$$\omega \simeq \frac{\mu_d}{\sqrt{2\mathfrak{h}}} \left( e^{-\sqrt{2\mathfrak{h}}|ka|} - 1 \right) n. \quad (43)$$

Note that the usual dispersion relation for nodal waves in an infinitesimally thin disk,  $\omega \simeq -\mu_d|ka|n$ , is obtained when  $\mathfrak{h} \rightarrow 0$ .

The dimensionless form of the dispersion relation is

$$\omega_i(K) = e^{-K} - 1, \quad (44)$$

where  $\omega_i = \sqrt{2\mathfrak{h}}\omega/\mu_d n$ , which is plotted in Figure 1. As the Figure shows, nodal bending waves can propagate only in regions where  $-1 < \omega_i(a) < 0$  which similarly limits the disk thickness to  $\mathfrak{h} \lesssim 2.72\mathfrak{h}_Q$ . The nodal waves’ group velocity is

$$c_g = \frac{d\omega}{dk} = -s_k \mu_d (1 + \omega_i) n a, \quad (45)$$

which indicates that nodal waves tend to stall, *i.e.*,  $|c_g| \rightarrow 0$  as they approach the  $\omega_i = -1$  boundary. Note that this dispersion relation only admits a long wavelength solution having a wavenumber  $|k_L| \simeq -\omega/\mu_d n a$  and a wavelength  $\lambda_L \simeq 2\pi\mu_d|n/\omega|a$  for waves far from the stall-zone. Since  $\mathfrak{h} \lesssim 2.72\mathfrak{h}_Q$ , the disk can sustain nodal waves wherever  $\lambda_L \gtrsim 9h$ . But if an outward-traveling long leading wave with  $s_k = -1$  encounters a disk edge, it will reflect as an  $s_k = +1$  long trailing wave. Examples of nodal wave reflection and stalling are also given below.

#### 4. The Secular Evolution of the Primordial Kuiper Belt

Using the recipe given in Section 2.1.1, the rings model is used to compute the secular evolution of the primordial Kuiper Belt as it is perturbed by the four giant planets. In these simulations the giant planets are represented by thin  $\mathfrak{h} = 0$  rings whose initial orbits are their current orbits, while the Kuiper Belt is represented by 500 rings whose semimajor axes extend from 36 AU out to 50–70 AU. The location of the Belt’s inner edge is chosen such that only the outermost radial and vertical secular resonances, the  $\nu_8$  and the  $\nu_{18}$ , reside in this disk near 40 AU when of low mass. The semimajor axes of each Belt-ring increases as  $a_{j+1} = (1 + \delta)a_j$  where the rings’ fractional separation  $\delta$  is typically  $\sim 0.001$ . The rings fractional half-thickness  $\mathfrak{h}$  is always in excess of  $2\delta$ , as is required to get the correct apse

precession in an axisymmetric disk (see Section 2.2.3). The Belt–rings initial eccentricities and inclinations are zero, with all inclinations being measured with respect to the system’s invariable plane. The mass of each ring is chosen such that the Belt’s surface density  $\sigma(a)$  varies as  $a^{-1.5}$ . For this configuration, if the total Kuiper Belt mass over the  $36 \leq a \leq 70$  AU zone is  $M_{\text{total}}$ , then the total mass in the ‘observable’  $30 \leq a \leq 50$  AU zone that is presently accessible to astronomers would be  $M_{KB} = 0.67M_{\text{total}}$  had the above surface density law extended inwards to 30 AU. For these systems the normalized disk mass is  $\mu_d \simeq M_{KB}/M_{\odot}$ .

#### 4.1. A $M_{KB} = 10 M_{\oplus}$ Example

Figure 2 shows a snapshot of apsidal density waves as they propagate across an  $M_{KB} = 10 M_{\oplus}$  Kuiper Belt having a half–thickness  $\mathfrak{h} = 5\delta = 0.0067$ . Since  $\mathfrak{h} \sim 0.2\mathfrak{h}_Q$ , the necessary disk–conditions for the propagation of apsidal and nodal waves are well–satisfied. Initially, a long trailing density wave is launched at the Belt’s inner edge. This wave is really more like a pulse  $\sim 5$  AU wide, and Figure 2 shows that by time  $t = 2 \times 10^6$  years the wave has just started to reflect at the disk’s outer edge at 70 AU. The greyscale map of the disk’s surface density variation,  $\Delta\sigma/\sigma$ , is obtained using equation (39), and this map also provides a historical record of this system’s wave–action. It should be noted that equation (39) is quantitatively correct only when  $|\Delta\sigma/\sigma| \ll 1$ , a condition that is rarely satisfied by the results obtained here. Nonetheless, equation (39) is still useful in a qualitative sense since it will indicate the disk–regions where large surface density variations as well as orbit–crossing can be expected. As the outer edge of the  $\Delta\sigma/\sigma$  map shows, the main apsidal density wave–pulse at  $67 < a < 70$  AU has just reflected at a short trailing wave, and this nonlinear wave having  $|\Delta\sigma/\sigma| > 1$  will completely dominate the disk’s appearance at later times as it propagates inwards. But until this happens, the bulk of the disk’s appearance over  $45 < a < 67$  AU is still dominated by lower–amplitude long waves that are following behind the main density pulse. Note also that short leading waves were also emitted at the disk’s inner edge, but as the density greyscale shows, they have only propagated out to  $a = 45$  AU thus far owing to their slower group velocity [see equation (38)]. These short waves are well–resolved in the sense that their radial wavelength of  $\lambda_S \sim 1$  AU spans about 15 disk–rings. Although these short waves are seen in the  $e(a)$  and  $\tilde{\omega}(a)$  plots as only tiny wiggles over  $36 < a < 45$  AU that are superimposed on top of the disk’s longer–wavelength behavior, the density greyscale shows that the short waves dominate the inner disk’s appearance. The online edition of Fig 2 is also linked to an animated sequence of these figures that give the system’s complete time–history. That animation shows that by time  $t \simeq 1 \times 10^7$  years, nonlinear short waves will have swept across the entire disk, and they result in large surface density variations  $|\Delta\sigma/\sigma| > 1$  over radial wavelengths of  $\lambda_S \sim 1$  AU.

Figure 2 also shows that by time  $t = 2 \times 10^6$  years, a long leading nodal bending wave–pulse has already propagated across the disk where it has reflected at the disk’s outer edge and just started to return inwards as a long trailing bending wave. But when that pulse reaches the disk’s inner edge, a portion of the wave’s angular momentum content will continue to propagate further inwards where it will give a small kick to the giant planets’ orbit elements, while the remaining wave–pulse reflects again and propagates outwards. The same phenomenon also occurs among the apsidal density waves. Thus after a few reflections, a single wave–pulse will lose its initial spatial coherence by spawning multiple wave–trains that, in this friction–free model, forever roam about the Belt. This ultimately results in a rather wobbly–looking standing density wave pattern that varies over the short wavelength scale  $\lambda_S \sim 1$  AU, as well as a standing bending wave pattern that varies over a much longer scale  $\lambda_L \sim 40$  AU.

A dynamical ‘spectrum’ of this Kuiper Belt is shown in Figure 3, which plots all of the eccentricity eigenvector elements  $|E_{ji}|$  for each of the disk–rings versus their eigenfrequency  $g_i$ , as well as inclination eigenvector elements  $|I_{ji}|$  versus eigenfrequency  $|f_i|$ . The upper figure is quite reminiscent of the findings of Tremaine (2001), who showed that a gravitating disk tends to exhibit its strongest response to slow radial perturbations via modes having discrete patterns speeds  $\omega$  that can be identified with any of the peak frequencies  $g_i$  seen in Figure 3. Figures such as these are quite useful for identifying the patterns speeds  $\omega$  that are associated with the density and bending waves that propagate in the disk.

#### 4.2. Variations with Kuiper Belt Mass $M_{KB}$

Simulations have been performed with Kuiper Belts having masses  $M_{KB} = 0, 0.08, 0.2, 2, 10,$  and  $30 M_{\oplus}$  in the observable  $30 \leq a \leq 50$  AU zone (again this would be the Belt’s mass assuming its surface density  $\sigma(a) \propto a^{-1.5}$  were to extend solely over that region). The results are summarized in Figure 4 which shows the maximum eccentricities  $e_{\max}$  and maximum inclinations  $i_{\max}$  achieved by the rings in each simulation. The Belt’s radial width is indicated by the breadth of the curves in Figure 4, which ranges from 34 AU in the higher–mass Belts to 14 AU for the  $M_{KB} = 0.08 M_{\oplus}$  system. Each simulation uses 500 disk–rings having a fractional half–thickness  $\mathfrak{h} = 2\delta$ , so the three higher–mass systems have  $\mathfrak{h} = 0.0027$  while the lower–mass disk  $M_{KB} = 0.2 M_{\oplus}$  is somewhat thinner with  $\mathfrak{h} = 0.0015$  and the  $M_{KB} = 0.08 M_{\oplus}$  system has  $\mathfrak{h} = 0.0010$ . The rings in these lower–mass disks are more closely packed so that their shorter–wavelength density waves are well resolved, and they are also made thinner so as to push their  $Q$ –barriers a bit further downstream. The disk’s initial orbits are  $e = 0 = i$ , except for the  $M_{KB} = 0$  system which instead

adopts the forced orbit elements appropriate for a massless disk [e.g., Brouwer & Clemence (1961); Murray & Dermott (1999)]. These systems are evolved until their initial density and bending wave pulses have had the opportunity to reflect multiple times and have largely dissolved into standing wave patterns. The lower-mass disks necessarily have longer run-times due to their waves’ slower propagation speeds [see equation (38)]; these run-times are  $1 \times 10^9$  years,  $2 \times 10^9$  years,  $1 \times 10^8$  years,  $2 \times 10^7$  years, and  $1 \times 10^7$  years, respectively, for the  $M_{KB} = 0.08, 0.2, 2, 10,$  and  $30 M_{\oplus}$  systems. Once the standing wave pattern has emerged, the rings’ instantaneous eccentricities and inclinations range over  $0 \lesssim e < e_{\max}$  and  $0 \lesssim i < i_{\max}$ .

As Figure 4 shows, there are no peaks in the  $e_{\max}$  and  $i_{\max}$  curves for the higher mass disks having  $M_{KB} \geq 2 M_{\oplus}$ , indicating that there are no secular resonances in the disk itself; any such resonances likely lie between the orbits of Neptune and the disk’s inner edge at 36 AU. The simulations of these higher-mass disks show long trailing density waves and long leading bending waves being launched at the disk’s inner edge. These waves sweep across the disk, reflect at the disk’s outer edge, and return as short trailing density waves and long trailing bending waves, similar to the history described in Section 4.1 and seen in Figure 2.

However secular resonances at  $a \simeq 41$  AU are quite prominent in the lower-mass disks having  $M_{KB} = 0.08$  and  $0.2 M_{\oplus}$ . These are sites that launch long density and bending waves, and as Figure 2 shows, the density waves are able to propagate out as far as  $a = 45$  and  $49$  AU, respectively, where they are reflected by a  $Q$ -barrier and return as short density waves. These reflection sites occur where  $\mathfrak{h} \simeq 2.2\mathfrak{h}_Q$  and  $\mathfrak{h} \simeq 1.4\mathfrak{h}_Q$ , which shows that equation (37) is an approximate yet useful indicator of where apsidal wave are allowed to propagate. Note also the large amplitudes of the density waves in these low-mass disks,  $0.3 \lesssim e_{\max} \lesssim 1$ , which clearly violates the model’s assumption of low eccentricities. Thus these particular curves should not be taken at face value. Nonetheless, they do indicate that apsidal waves in a low-mass Kuiper Belt may result in large eccentricities, and Figure 2 shows that sizable inclinations can also result due to nodal bending waves. Indeed, in the  $M_{KB} = 0.08 M_{\oplus}$  disk, maximum inclinations are typically  $i \sim 20^\circ$ , which is comparable to the Main Belt’s high-inclination component.

The larger  $e$ ’s and  $i$ ’s seen in the lower-mass disk’s are a consequence of the giant planets transmitting a small fraction of their initial angular momentum deficit<sup>4</sup> (AMD) into the disk in each simulation. In each simulation, the giant planets deposit  $\sim 0.005L_e$  and  $\sim 0.1L_i$  into the disk’s inner edge, which waves then transport and smear out across a vast swath of the Kuiper Belt. Since the AMD deposited in the disk is roughly constant in

---

<sup>4</sup>e.g., the  $L_e$  and  $L_i$  of equations (26).

each simulation, the lower-mass disks exhibit larger  $e$  and  $i$  excitations. It should also be noted that computational limitations in dynamical studies of the Kuiper Belt, particularly N-body simulations, are often require treating the Belt as a swarm of massless test particles. However the comparison of the  $M_{KB} = 0$  curve to the  $M_{KB} > 0$  curves in Figure 2 shows that the endstate of a Kuiper Belt having even just a modest amount of mass can be radically different from one naively treated as massless.

### 4.3. Variations with Disk Thickness $\mathfrak{h}$

Figure 5 shows how the response of an  $M_{KB} = 10 M_{\oplus}$  Belt varies with increasing disk thickness  $\mathfrak{h} = (2, 20, 30, 60, 100) \times \delta = (0.0027, 0.027, 0.04, 0.08, 0.13)$ . According to equation (37),  $\mathfrak{h}_Q(a) \propto a^{1/2-r=-1}$  in these  $r = 3/2$  disks, so the  $Q$ -barrier will move inwards as the disk's  $\mathfrak{h}$  is increased, as is evident in Figure 5. All of these disks have a normalized disk mass  $\mu_d \simeq 3 \times 10^{-5}$ , a mean motion  $n \simeq 0.02$  radians/year, and a pattern speed that is typically  $\omega \sim 3 \times 10^{-6}$  radians/year, so wave-action is shut off when the disk thickness  $\mathfrak{h}$  exceeds  $\mathfrak{h}_Q = 0.26\mu_d|n/\omega| \sim 0.05$ . In the thinnest disk with  $\mathfrak{h} = 0.0027$ , the  $Q$ -barrier lies beyond the disk's outer edge at 70 AU, so long and then short apsidal density waves are able to slosh about the disk's full extent. However the  $Q$ -barrier lies in the disk at  $a \simeq 60$  AU when  $\mathfrak{h} = 0.027$  (red curve), at  $a \simeq 53$  AU when  $\mathfrak{h} = 0.04$  (green curve), and apsidal waves are prohibited in the disks with  $\mathfrak{h} \geq 0.08$  (blue and purple curves).

Figure 5 also shows that the nodal bending waves are shut off when the disk thickness  $\mathfrak{h}$  exceeds the somewhat more relaxed criterion  $2.72\mathfrak{h}_Q \sim 0.14$ . Note also the peak at  $a \simeq 53$  AU in the  $\mathfrak{h} = 0.027$  disk (red curve) and at  $a \simeq 39$  AU in the  $\mathfrak{h} = 0.04$  disk (green curve). These particular disks admit two spiral patterns, a higher-amplitude spiral that corotates with Neptune's dominant eigenmode at the pattern speed of  $\omega \sim -3 \times 10^{-6}$  radians/year, and a lower-amplitude mode that corotates with Uranus at the faster rate  $\omega \sim -1.5 \times 10^{-5}$  radians/year. Since  $\mathfrak{h}_Q \propto |\omega|^{-1}$ , the faster spiral pattern has  $2.72\mathfrak{h}_Q \sim 0.03$ , which is why this wave stalls at  $a = 53(39)$  AU in the  $\mathfrak{h} = 0.027(0.04)$  disks while the slower spiral mode is able to propagate the full breadth of these disks.

The behavior of a lower-mass disk with  $M_{KB} = 0.2 M_{\oplus}$  is shown in Figure 6 for disks having  $\mathfrak{h} = (2, 5, 10, 15) \times \delta = (0.0015, 0.0037, 0.0074, 0.011)$ . A pair of secular resonances lie near  $a \simeq 40$  AU, and they launch apsidal and nodal waves having pattern speeds  $\omega \sim \pm 3 \times 10^{-6}$  radians/year. These disks have  $\mu_d \simeq 6 \times 10^{-7}$  and  $\mathfrak{h}_Q \sim 0.001$ , and as the upper plot shows, further increases in  $\mathfrak{h}$  brings the  $Q$ -barrier inwards until the wave-propagation zone has shrunk down to zero. The lower plot also shows that nodal waves forever slosh about the model Kuiper Belt in the  $\mathfrak{h} = 0.0015$  disk (orange curve), whereas the peaks in

the other curves show that these waves stall at sites ever closer to resonance in progressively thicker disks. These Figures also show that when  $\mathfrak{h} \gg \mathfrak{h}_Q$ , the motions of a non-gravitating disk are recovered, namely, the disk’s  $e$ ’s and  $i$ ’s are twice the forced motions seen in the  $M_{KB} = 0$  disk (black curves), with the factor of two being a consequence of these disks’ initial conditions  $e = 0 = i$ .

#### 4.4. Implications for the Primordial Kuiper Belt

The primordial Kuiper Belt likely had an initial mass of  $M_{KB} \sim 30 M_\oplus$  (see Section 1), and accretion models show that the initial KBO swarm must have had dispersion velocities less than  $\sim 0.001 \times$  Keplerian (Kenyon & Luu 1999), so  $\mathfrak{h} \lesssim 0.001$ ,  $\mu_d \sim 1 \times 10^{-4}$ , and thus  $\mathfrak{h}_Q \sim 0.2$  assuming the spiral waves have pattern speeds of  $|\omega| \sim 3 \times 10^{-6}$  radians/year. Since  $\mathfrak{h} < \mathfrak{h}_Q$ , the primordial Kuiper Belt readily sustained apsidal and nodal waves. Figure 4 shows that in this high-mass environment, these will be rather low-amplitude waves having  $e \sim \sin i \sim 0.01$ . These waves will quickly propagate across a Kuiper Belt of width  $\Delta a$  in time  $T_{\text{prop}} \sim \Delta a / |c_g| \simeq \Delta a / \mu_d a n$ , so the wave propagation time is

$$T_{\text{prop}} \sim 3 \times 10^5 \left( \frac{M_{KB}}{30 M_\oplus} \right)^{-1} \left( \frac{\Delta a}{30 \text{ AU}} \right) \text{ years.} \quad (46)$$

In the friction-free model employed here, the outward-bound long density waves eventually reflect, either at a  $Q$ -barrier in the disk (which might lie downstream where  $\mathfrak{h} = \mathfrak{h}_Q$ ) or else at the disk’s outer edge. The reflected waves then propagate inwards as short density waves, and such waves are nonlinear in the sense that their surface density variations  $\Delta\sigma/\sigma$  typically exceed unity. Figure 2 shows a snapshot of long and short density waves in a  $M_{KB} = 10 M_\oplus$  disk. Note that the long waves completely dominate the disk’s orbit elements  $e(a)$  and  $\tilde{\omega}(a)$  that vary over a wavelength of  $\lambda_L \sim 10$  AU, while the short waves are the tiny variations in  $e(a)$  and  $\tilde{\omega}(a)$  that occur over a  $\lambda_S \sim 1$  AU scale at the disk’s inner and outer edge. Even though the short waves are almost imperceptible in the orbit-elements plots, the greyscale map shows that these nonlinear short waves completely dominate the disk’s surface density structure.

Figure 4 also shows that the waves in lower-mass systems have higher amplitudes. This suggests that wave action may tend to drive disk-planet systems towards an equipartition of angular momentum deficits, since the angular momentum content of the waves seen in all simulations are  $\sim 0.5\%$  and  $\sim 10\%$  of the planets’  $L_e$  and  $L_i$ .

The large-amplitude waves seen in the  $M_{KB} = 0.2 M_\oplus$  disk also suggests that apsidal and nodal wave action might account for much of the Kuiper Belt’s excited state (see Figure



4). However the viability of this scenario depends critically upon the timescales that govern the Belt’s mass loss as well as the KBOs’ velocity evolution. First note that accretion models show that as soon as the large  $R \gtrsim 100$  km KBOs form, further KBO growth is halted as they initiate an episode of more vigorous collisions that steadily grind the Belt’s smaller members down to dust which radiation forces then transport away (Kenyon & Luu 1999; Kenyon & Bromley 2001). Accretion models show that the  $R \sim 100$  km KBOs form at  $a \sim 35$  AU over a  $\tau_{\text{form}} \sim 1 \times 10^7$  year timescale, and that the Belt’s subsequent collisional erosion occurs over a  $\tau_{\text{erode}} \sim 5 \times 10^8$  year timescale (Kenyon & Luu 1999; Kenyon & Bromley 2001). And if Neptune’s orbit had migrated substantially, the advancing 2:1 resonance would also have swept across the Main Belt, which further enhances the stirring as well the collisional/dynamical erosion. The resulting grinding and erosion thus makes it ever more difficult for the Belt to sustain waves as the initially massive Kuiper Belt mass is eroded by a factor of  $\sim 150$ , which also lowers the disk’s  $\mathfrak{h}_Q \rightarrow \sim 10^{-3}$ . Note that the removal of the smaller KBOs also turns off the dynamical friction that was once keeping the particle disk quite thin. The gravitational stirring by the surviving larger KBOs is then free to raise their dispersion velocities  $c$  up to their surface escape velocity  $v_{\text{esc}}$  (Safronov 1972), which results in a thicker disk with  $\mathfrak{h} \sim v_{\text{esc}}/na \sim 0.02(R/100 \text{ km})$  where  $R$  is the KBOs’ characteristic size. Since this is substantially larger than the current Belt’s  $\mathfrak{h}_Q$ , it seems quite likely that this stirring shut off the waves while they were still of low amplitude (see Fig. 4) long before the Kuiper Belt was ground down to its present mass<sup>5</sup>. Consequently, apsidal and nodal waves were likely able to propagate throughout the Kuiper Belt during a timescale  $\tau_{\text{wave}}$  that is bounded by the moment when the large KBOs first formed and when the Belt eroded away, *i.e.*,  $\tau_{\text{form}} < \tau_{\text{wave}} < \tau_{\text{erode}}$ .

#### 4.5. Comments on Studies of Spiral Waves in Galactic Disks

It should also be noted that this implementation of the rings model does not account for any viscous damping of spiral waves which, as Hunter & Toomre (1969) point out, may be more important as bending waves approach a disk’s outer edge. Unlike the sharp-edged disks employed here, a more realistic disk likely has a ‘fuzzy’ edge where the disk’s surface density gently tapers to zero. Hunter & Toomre (1969) show that bending waves entering

---

<sup>5</sup>An exception to this assertion might occur if the reflection of nodal waves at an outer edge allowed the Belt to behave as a resonant cavity (Ward 2003). When the disk’s mass and the wave’s pattern speed are appropriately tuned, which can occur naturally as the Belt eroded and/or the as Neptune’s precession rate varied due to its orbital migration, then a higher-amplitude standing wave pattern can result while the Belt persists in the tuned state.

such a lower-density zone tend to excite substantially larger inclinations there, and such sites will be considerably more susceptible to the viscous dissipation of these possibly nonlinear waves.

Toomre (1983) suggests that disks having a tapered edge might also cause bending waves to stall there since the group velocity  $c_g \rightarrow 0$  as the surface density  $\sigma$  smoothly goes to zero. However this assertion was not confirmed by the rings model, which tapered a disk’s outer surface density by multiplying it by the factor  $\sqrt{1 - (\ell - \Delta a)^2/\ell^2}$  where  $\Delta a$  is the distance from the outer edge and  $\ell$  is the tapering scale-length. These experiments adopt values of  $\ell$  that are smaller, comparable, and larger than the bending wavelength  $\lambda_L$ , and in all cases the bending wave reflects at or near the disk edge, with considerably larger inclinations being excited in this tapered zone.

## 5. Summary

A model that rapidly computes the secular evolution of a gravitating disk–planet system is developed. The disk is treated as a nested set of rings, with the rings’/planets’ time–evolution being governed by the Lagrange planetary equations. It is shown that the solution to the dynamical equations is a modified version of the classical Laplace–Lagrange solution for the secular evolution of the planets (Brouwer & Clemence 1961; Murray & Dermott 1999), with the modification being due to a ring’s finite thickness  $h = c/n$  that is a consequence of the dispersion velocity  $c$  of that ring’s constituent particles. Since the ring’s finite thickness  $h$  softens its gravitational potential, this also softens the Laplace coefficients appearing in the Laplace–Lagrange solution over a scale  $h/a$ .

It is shown that the Lagrange planetary equations admit spiral wave solutions when the tight–winding approximation is applied. There are two types of spiral density (or apsidal) waves, long waves of wavelength  $\lambda_L = 2\pi\mu_d|n/\omega|a$  and short waves of wavelength  $\lambda_S < 2\sqrt{2}\pi\mathfrak{h}a$  where  $\mathfrak{h} = h/a$  is the disk’s fractional thickness and  $\omega$  is the angular rate at which the spiral pattern rotates. The simulations presented here show that the giant planets launch long waves at either a resonance in the disk or else at the disk’s nearest edge, and that these waves propagate away until they reflect at the disk’s far edge or else at a  $Q$ –barrier in the disk which resides where  $\mathfrak{h} = \mathfrak{h}_Q(a)$  where  $\mathfrak{h}_Q(a) = 0.26\mu_d|n/\omega|$  is the maximum disk thickness that can sustain apsidal waves, with  $\mu_d = \pi\sigma a^2/M_\odot$  being the normalized disk mass. Of course all of these findings may be derived from the stellar dispersion relation given in Toomre (1969) in the limit that the pattern speed  $\omega$  is much smaller than the disk’s mean motion  $n$ . Nonetheless, it is satisfying to see that the theory of unforced apsidal waves is readily obtained from the Lagrange planetary equations; with a little more effort

the theory for forced apsidal waves [e.g., Ward & Hahn (1998)] should also be recoverable.

However new results are obtained for the nodal wave problem, which admits only a long-wavelength solution  $\lambda_L$  to the planetary equations in the tight-winding limit. In particular, it is shown that these waves can stall, that is, the waves' group velocity plummets to zero as they approach a site in the disk where  $\mathfrak{h} = 2.72\mathfrak{h}_Q$ . If, however, these waves instead encounter a disk edge, they will reflect and return as long waves. In the limit that  $\mathfrak{h} \rightarrow 0$ , the results for nodal waves propagating in an infinitesimally thin disk is recovered (Ward & Hahn 2003), but note that the wave-stalling phenomenon does not appear in a  $\mathfrak{h} = 0$  treatment of the disk.

The rings model is also used to examine the propagation of apsidal and nodal waves that are launched by the giant planets into a variety of Kuiper Belts having a mass  $M_{KB} = 30 M_\oplus$  (the estimated primordial mass) down to  $M_{KB} = 0.08 M_\oplus$  (which is  $\sim 40\%$  of the Belts current mass estimate). In each simulation the giant planets deposit roughly the same fraction of their initial angular momentum deficits,  $\sim 0.5\%$  and  $\sim 10\%$  of the planets'  $L_e$  and  $L_i$ , into the disk in the form of spiral waves. And since the waves' angular momentum content is roughly the same in each simulation, the lower-mass Kuiper Belts thus experience higher-amplitude waves. Indeed, the waves seen in the  $M_{KB} \leq 0.2 M_\oplus$  simulations are of sufficient amplitude that they could in principle account for much of the dynamical excitation that is observed in the Kuiper Belt. However wave-action in a  $M_{KB} \sim 0.2 M_\oplus$  Belt also requires its fractional scale-height to quite thin, namely,  $\mathfrak{h} \lesssim 10^{-3}$ . Most likely, apsidal and nodal waves were shut off, due to self-stirring by large KBOs as well as by other external perturbations, long before the Belt eroded down to its current mass, in which case the excitation by wave-action would have been quite modest.

The rings model developed here has many other applications. One issue of great interest is to determine whether apsidal and nodal waves may be propagating in Saturn's rings. Of particular interest are the short apsidal waves since their detection could yield the ring's dispersion velocity  $c$  via a measurement of the short wavelength  $\lambda_S \sim 9c/n$ . Although the ring particles' dispersion velocity is of fundamental importance to ring dynamics, it is less than well constrained at Saturn. Of course, the differential precession due to planetary oblateness also needs to be included in the model [c.f., Murray & Dermott (1999)] since this effect may actually defeat this form of wave-action. The rings model can also be used to examine the forced motions of a relatively massless but much thicker circumstellar dust disk like  $\beta$  Pictoris. The warps and brightness asymmetries seen in this system are usually attributed to secular perturbations exerted by an unseen planetary system, and the code developed here can be used to very rapidly explore the wide range of planetary parameters. This rings model will be used to study these and other problems in greater detail in the near

future.

## ACKNOWLEDGMENTS

This paper is contribution XXXX from the Lunar and Planetary Institute, which is operated by the Universities Space Research Association by cooperative agreement NCC5–679 with the National Aeronautics and Space Administration. This research was also supported by NASA via the Origins of Solar Systems grant No. NAG5–10946 issued through the Office of Space Science.

## A. Appendix A

Differentiating the  $\tilde{b}_s^{(m)}$  appearing in the  $f$  and  $g$  functions, equations (17), yields

$$f = 2\alpha\tilde{b}_{3/2}^{(1)} + \frac{3}{2}\alpha^2 \left( \tilde{b}_{5/2}^{(2)} - \tilde{b}_{5/2}^{(0)} \right) - 3\alpha^2 H^2 (2 + H^2) \tilde{b}_{5/2}^{(0)} \quad (\text{A1a})$$

$$g = 2(\alpha^2 + 1)(1 + H^2)\tilde{b}_{3/2}^{(1)} - 3\alpha \left( \tilde{b}_{3/2}^{(0)} + \tilde{b}_{3/2}^{(2)} \right) + 3\alpha^2 H^2 (2 + H^2) \tilde{b}_{5/2}^{(1)} - \frac{3}{4}\alpha^2 \left( \tilde{b}_{5/2}^{(3)} - \tilde{b}_{5/2}^{(1)} \right) \quad (\text{A1b})$$

where  $H^2 = \frac{1}{2}(\mathfrak{h}^2 + \mathfrak{h}'^2)$ . The following recursion relations,

$$m\tilde{b}_s^{(m)} = s\alpha \left( \tilde{b}_{s+1}^{(m-1)} - \tilde{b}_{s+1}^{(m+1)} \right) \quad (\text{A2a})$$

$$(m + 1 - s)\alpha\tilde{b}_s^{(m+1)} = m(1 + \alpha^2)(1 + H^2)\tilde{b}_s^{(m)} - (m + s - 1)\alpha\tilde{b}_s^{(m-1)}, \quad (\text{A2b})$$

can be used to simplify equations (A1) further. Equations (A2) are derived in Brouwer & Clemence (1961) for the case where  $H = 0$ . However the more general relations given above are readily obtained by replacing the combination  $1 + \alpha^2$  appearing in the Brouwer & Clemence (1961) recursion relations with  $(1 + \alpha^2)(1 + H^2)$ . So for  $m = 1$  and  $s = 3/2$  equation (A2a) is

$$\tilde{b}_{3/2}^{(1)} = \frac{3}{2}\alpha \left( \tilde{b}_{5/2}^{(0)} - \tilde{b}_{5/2}^{(2)} \right) \quad (\text{A3})$$

and

$$\tilde{b}_{3/2}^{(2)} = \frac{3}{4}\alpha \left( \tilde{b}_{5/2}^{(1)} - \tilde{b}_{5/2}^{(3)} \right) \quad (\text{A4})$$

for  $m = 2$  and  $s = 3/2$  while equation (A2b) yields

$$2(\alpha^2 + 1)(1 + H^2)\tilde{b}_{3/2}^{(1)} = \alpha\tilde{b}_{3/2}^{(2)} + 3\alpha\tilde{b}_{3/2}^{(0)} \quad (\text{A5})$$

for  $m = 1$  and  $s = 3/2$ . Inserting equations (A3–A5) into (A1) then yields

$$f(\alpha, \mathfrak{h}, \mathfrak{h}') = \alpha\tilde{b}_{3/2}^{(1)} - 3\alpha^2 H^2 (2 + H^2) \tilde{b}_{5/2}^{(0)} \quad (\text{A6a})$$

$$g(\alpha, \mathfrak{h}, \mathfrak{h}') = -\alpha\tilde{b}_{3/2}^{(2)} + 3\alpha^2 H^2 (2 + H^2) \tilde{b}_{5/2}^{(1)}. \quad (\text{A6b})$$

## B. Appendix B

The symbolic mathematics software MAPLE has been used to write the needed softened Laplace coefficients  $\tilde{b}_s^{(m)}$ , equation (12), in term of complete elliptic integrals  $K$  and  $E$ .

Setting  $H^2 = \frac{1}{2}(\mathfrak{h}^2 + \mathfrak{h}'^2)$ ,  $\gamma = (1 + \alpha^2)(1 + H^2)/2\alpha$ , and  $\chi = \sqrt{2/(\gamma + 1)}$ , then

$$\tilde{b}_{1/2}^{(0)}(\alpha, \mathfrak{h}, \mathfrak{h}') = \frac{4K(\chi)}{\pi\sqrt{2\alpha(\gamma + 1)}} \quad (\text{B1a})$$

$$\tilde{b}_{1/2}^{(1)}(\alpha, \mathfrak{h}, \mathfrak{h}') = \frac{4[\gamma K(\chi) - (\gamma + 1)E(\chi)]}{\pi\sqrt{2\alpha(\gamma + 1)}} \quad (\text{B1b})$$

$$\tilde{b}_{3/2}^{(0)}(\alpha, \mathfrak{h}, \mathfrak{h}') = \frac{2E(\chi)}{\pi\alpha(\gamma - 1)\sqrt{2\alpha(\gamma + 1)}} \quad (\text{B1c})$$

$$\tilde{b}_{3/2}^{(1)}(\alpha, \mathfrak{h}, \mathfrak{h}') = \frac{2[-(\gamma - 1)K(\chi) + \gamma E(\chi)]}{\pi\alpha(\gamma - 1)\sqrt{2\alpha(\gamma + 1)}} \quad (\text{B1d})$$

$$\tilde{b}_{3/2}^{(2)}(\alpha, \mathfrak{h}, \mathfrak{h}') = \frac{2[-4\gamma(\gamma - 1)K(\chi) + (4\gamma^2 - 3)E(\chi)]}{\pi\alpha(\gamma - 1)\sqrt{2\alpha(\gamma + 1)}} \quad (\text{B1e})$$

$$\tilde{b}_{5/2}^{(0)}(\alpha, \mathfrak{h}, \mathfrak{h}') = \frac{4[-(\gamma - 1)K(\chi) + 4\gamma E(\chi)]}{3\pi(2\alpha)^{5/2}(\gamma + 1)^{3/2}(\gamma - 1)^2} \quad (\text{B1f})$$

$$\tilde{b}_{5/2}^{(1)}(\alpha, \mathfrak{h}, \mathfrak{h}') = \frac{4[-\gamma(\gamma - 1)K(\chi) + (\gamma^2 + 3)E(\chi)]}{3\pi(2\alpha)^{5/2}(\gamma + 1)^{3/2}(\gamma - 1)^2} \quad (\text{B1g})$$

where

$$K(\chi) = \int_0^1 \frac{dt}{\sqrt{(1-t^2)(1-\chi^2 t^2)}} \quad (\text{B2})$$

is the complete elliptic integral of the first kind and

$$E(\chi) = \int_0^1 \sqrt{\frac{1-\chi^2 t^2}{1-t^2}} dt \quad (\text{B3})$$

is the complete elliptic integral of the second kind. The series expansions for  $K(\chi)$  and  $E(\chi)$  given in Abramowitz and Stegun (1970) then permit the rapid calculation of the softened Laplace coefficients  $\tilde{b}_s^{(m)}$  without requiring a numerical integration of equation (12). However equations (B1) can give unreliable results for extreme values of  $\alpha$  due to numerical roundoff errors. In this case it is preferable to factor the  $(1 + \alpha^2)(1 + H^2) = 2\alpha\gamma$  term out of the integrand in (12) and expand the denominator for the case of large  $\gamma \gg 1$ :

$$\tilde{b}_s^{(m)} = \frac{2}{\pi(2\alpha\gamma)^s} \int_0^\pi d\phi \cos(m\phi) \left[ 1 + \frac{s}{\gamma} \cos \phi + \frac{s(s+1)}{2\gamma^2} \cos 2\phi + \dots \right] \quad (\text{B4a})$$

$$\simeq \frac{f_m \alpha^m}{(2\alpha\gamma)^{s+m}} \quad (\text{B4b})$$

where  $f_0 = 2$ ,  $f_1 = 2s$ , and  $f_2 = s(s+1)$ . Equation (B4b) usually gives the more reliable result for  $\alpha \ll 0.01$  and for  $\alpha \gg 100$ .

Another useful form for  $\tilde{b}_s^{(m)}$  is obtained for regions where  $\alpha = 1 + x$  where  $|x| \ll 1$ . In this ‘local’ approximation, the dominant contribution to the integral, equation (12), occurs where  $\phi \ll 1$ . Thus we can set  $\cos \phi \simeq 1 - \phi^2/2$  and  $\alpha \simeq 1$  except where it appears as  $\alpha - 1 = x$ , extend the upper integration limit to infinity, and set  $\cos(m\phi) \simeq 1$  in the numerator [cf. Goldreich & Tremaine (1980)]:

$$\tilde{b}_s^{(m)}(x) \simeq \frac{2}{\pi} \int_0^\infty \frac{d\phi}{(x^2 + 2H^2 + \phi^2)^s} = \begin{cases} \frac{2/\pi}{x^2 + 2H^2} & \text{for } s = 3/2 \\ \frac{4/3\pi}{(x^2 + 2H^2)^2} & \text{for } s = 5/2 \end{cases} \quad (\text{B5})$$

### C. Appendix C

The time derivatives of  $L_e$ , equation (26a), is

$$\frac{dL_e}{dt} = \sum_j m_j n_j a_j^2 \left( h_j \frac{dh_j}{dt} + k_j \frac{dk_j}{dt} \right) \quad (\text{C1a})$$

$$= \sum_j \sum_{k \neq j} m_j n_j^2 a_j^2 A_{jk} (h_j k_k - h_k k_j) \quad (\text{C1b})$$

$$= \sum_j \sum_{k \neq j} \frac{1}{4} \left( \frac{m_j m_k}{M_\odot + m_j} \right) n_j^2 a_j^2 g_{jk} (h_j k_k - h_k k_j) \quad (\text{C1c})$$

where  $g_{jk} = g(\alpha_{jk}, \mathbf{h}_j, \mathbf{h}_k)$ . Let  $dL_e/dt = S_1 - S_2$  where  $S_1$  is the sum over the  $h_j k_k$  terms and  $S_2$  the sum over the  $h_k k_j$ . Swap the  $j$  and  $k$  indices in  $S_2$  so that it becomes

$$S_2 = \sum_k \sum_{j \neq k} \frac{1}{4} \left( \frac{m_k m_j}{M_\odot + m_k} \right) n_k^2 a_k^2 g_{kj} h_j k_k. \quad (\text{C2})$$

Equation (18c) shows that  $g_{kj} = \alpha_{jk} g_{jk}$ , and with  $(n_k/n_j)^2 = \alpha_{jk}^{-3} (M_\odot + m_k)/(M_\odot + m_j)$ ,  $S_2$  becomes

$$S_2 = \sum_k \sum_{j \neq k} \frac{1}{4} \left( \frac{m_j m_k}{M_\odot + m_j} \right) n_j^2 a_j^2 g_{jk} h_j k_k \quad (\text{C3})$$

which is  $S_1$  since the sums obey  $\sum_k \sum_{j \neq k} = \sum_j \sum_{k \neq j}$ . Consequently  $dL_e/dt = S_1 - S_2 = 0$ , and a similar analysis will also show that  $dL_i/dt = 0$ .

## REFERENCES

- Abramowitz, M. & Stegun, I. 1970, Handbook of Mathematical Functions, (New York: Dover Publications)
- Borderies, N., Goldreich, P. & Tremaine, S. 1985, *Icarus*, 63, 406.
- Brouwer, D. & Clemence, G. 1961, Methods of Celestial Mechanics, (New York: Academic Press)
- Brown, M. E. 2001, *AJ*, 121, 2804
- Chiang, E. I. & Jordan, A. B. 2002, *AJ*, 124, 3430
- Dermott, S. & Nicholson, P. 1986, *Nature*, 319, 115
- Duncan, M. J. & Levison, H. F. 1997, *Science*, 276, 1670
- Fernandez, J. A. & Ip, W.-H. 1984, *Icarus*, 58, 109
- Goldreich, P. & Tremaine, S. 1980, *ApJ*, 241, 425
- Gomes, R. 2003, *Icarus*, 161, 404
- Hahn, J. M., Ward, W. R., & Rettig, T. W. 1995, *Icarus*, 117, 25.
- Hahn, J. M. & Malhotra, R. 1999, *AJ*, 117, 3041
- Hahn, J. M. & Ward, W. R. 2002, Lunar and Planetary Science Conference XXXIII, abstract 1930
- Heppenheimer, T. A. 1980, *Icarus*, 41, 76
- Hunter, C. & Toomre, A. 1969, *ApJ*, 155, 747
- Jacobs, V. & Sellwood, J. A. 2001, *ApJ*, 555, L25
- Jewitt, D., Luu, J., & Trujillo, C. 1998, *AJ*, 115, 2125
- Kenyon, S. J. & Luu, J. X. 1999, *AJ*, 118, 1101
- Kenyon, S. J. & Bromley, B. C. 2001, *AJ*, 121, 538
- Malhotra, R. 1995, *AJ*, 110, 420



- Murray, C. & Dermott, S. 1999, *Solar System Dynamics*, (Cambridge, UK: Cambridge University Press)
- Nagasawa, M. & Ida, S. 2000, *AJ*, 120, 3311
- Safronov, V. S. 1972, NASA TT F-677
- Thommes, E. W., Duncan, M. J., & H. F. Levison. 2002, *AJ*, 123, 2862
- Toomre, A. 1969, *ApJ*, 158, 899
- Toomre, A. 1983, Theories of WARPS, in *Internal Kinematics and Dynamics of Galaxies*, IAU Symp. 100, 177
- Tremaine, S. 2001. *ApJ*, 121,1776
- Ward, W. R. 1981, *Icarus*, 47, 234
- Ward, W. R. & Hahn, J. M. 1998, *AJ*, 116, 489
- Ward, W. R. & Hahn, J. M. 1998, *Science*, 280, 2104
- Ward, W. R. & Hahn, J. M. 2003, *AJ*, in press
- Ward, W. R. 2003, *ApJ*, 584, L39

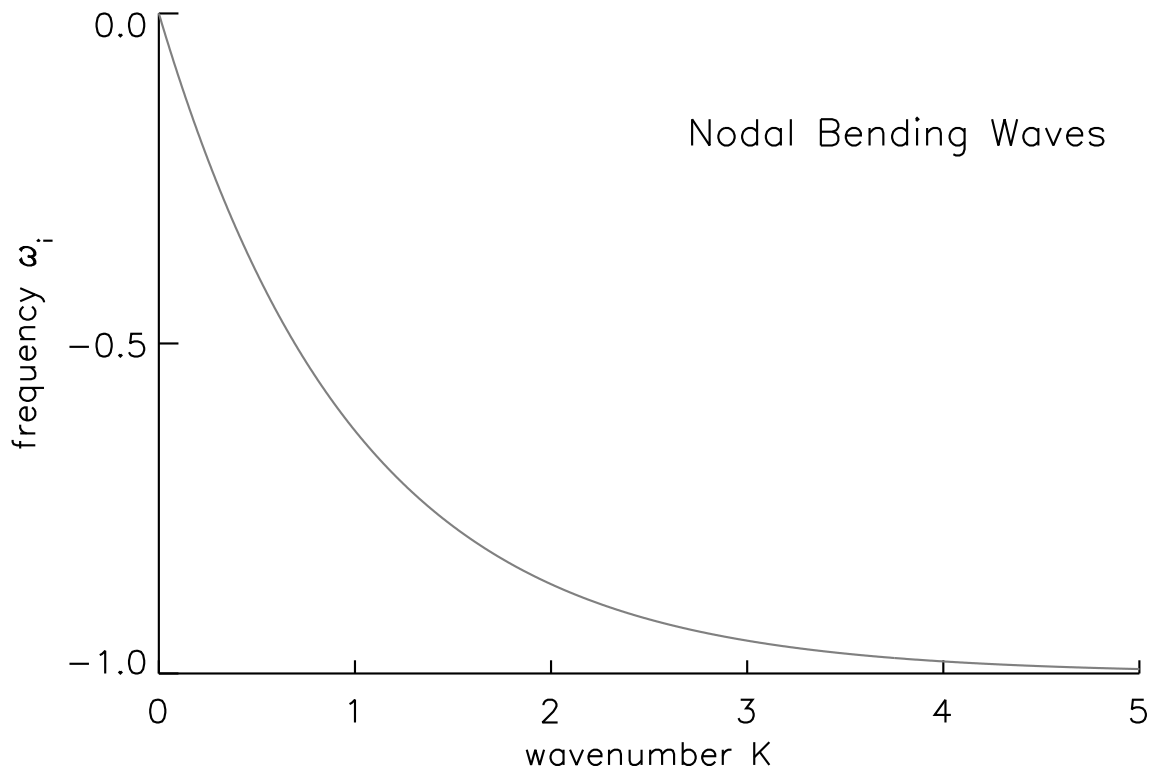
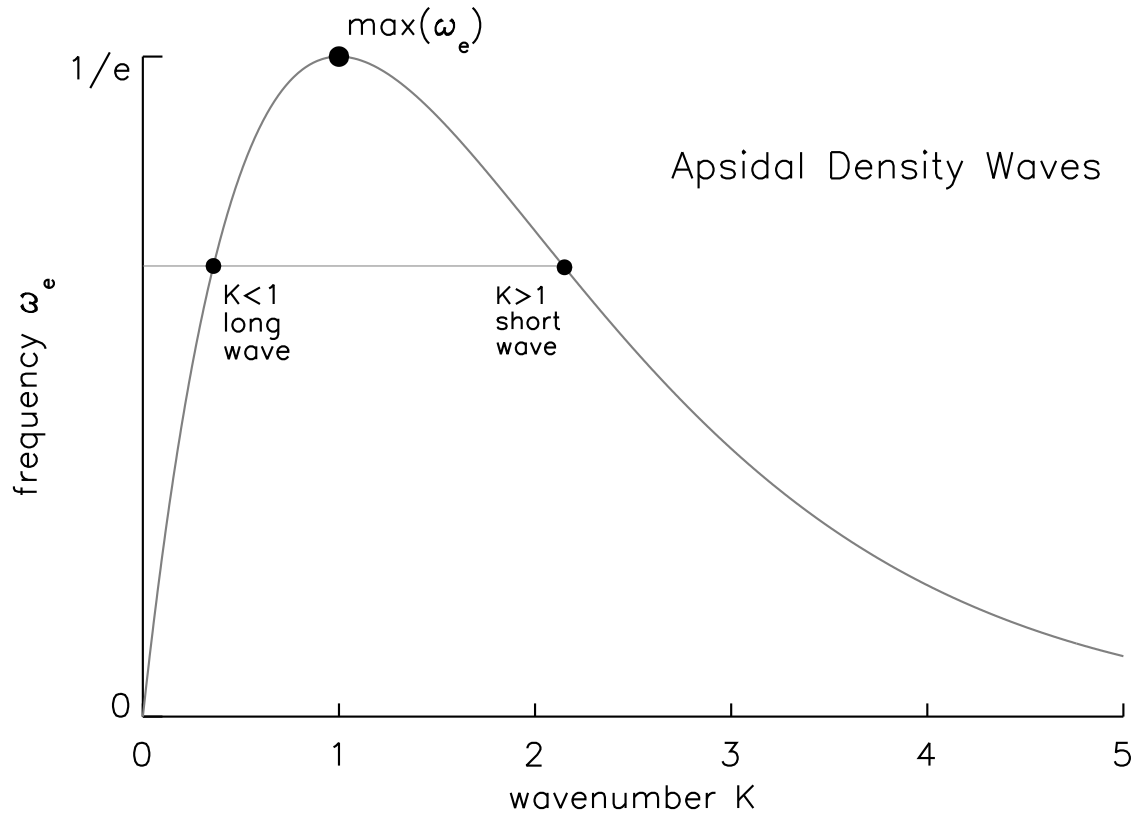


Fig. 1.— The upper figure is the dispersion relation  $\omega_e = Ke^{-K}$  for apsidal density waves, and the lower figure in the dispersion relation  $\omega_i = e^{-K} - 1$  for nodal bending waves.

time =  $2.00 \times 10^6$  years

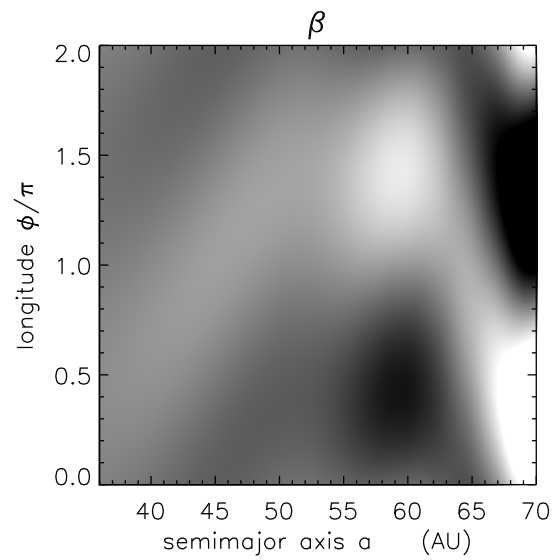
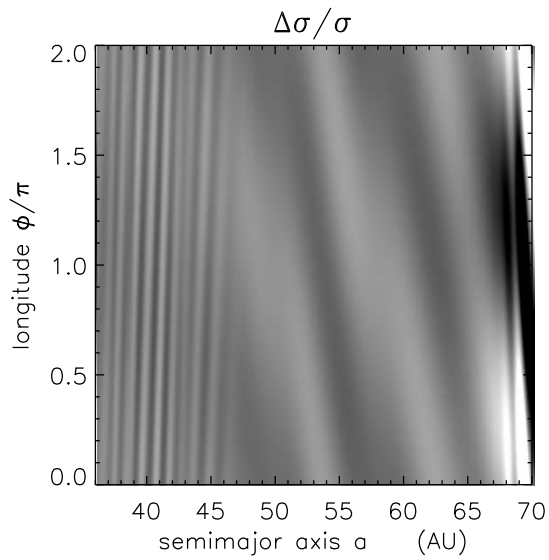
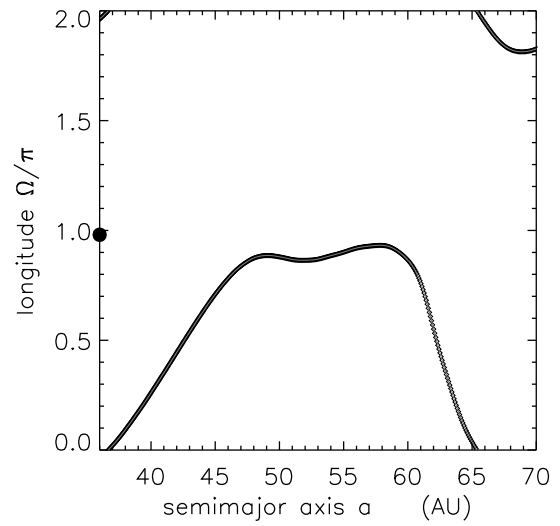
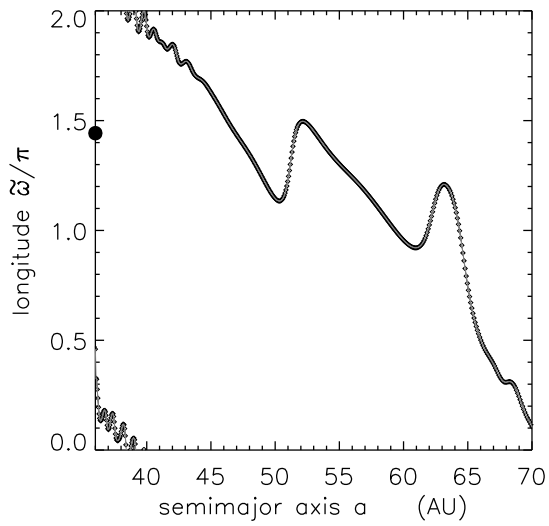
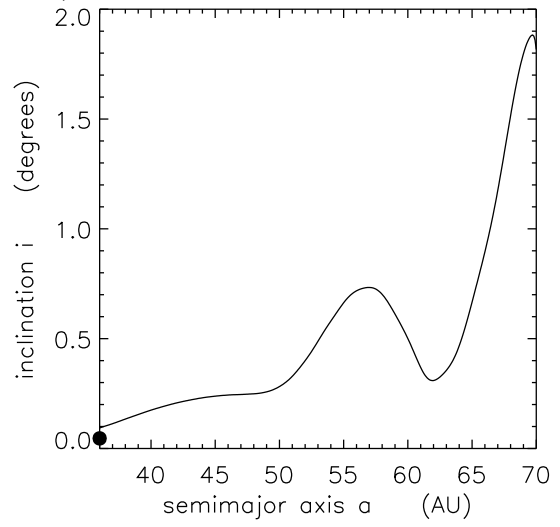
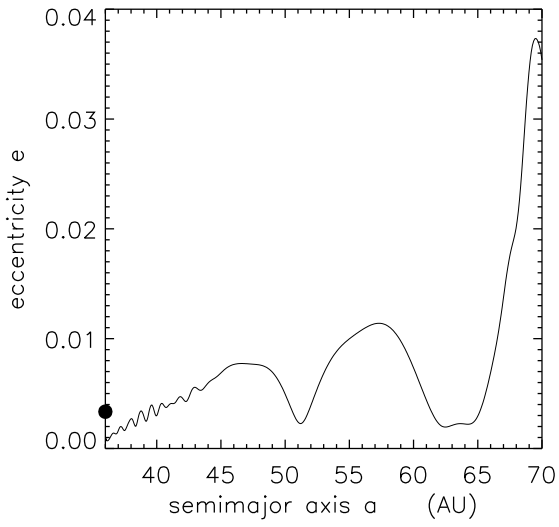


Fig. 2.— A snapshot of the simulated Kuiper Belt’s orbit elements  $(e, i, \tilde{\omega}, \Omega)$  plotted versus semimajor axis  $a$  at time  $t = 2 \times 10^6$  years in a  $M_{KB} = 10 M_{\oplus}$  Belt. The Belt’s fractional half-thickness is  $\mathfrak{h} = 0.0067$ . The dots along the left axes indicate Neptune’s orbit elements. The  $\Delta\sigma/\sigma$  greyscale shows the disk’s fractional surface density variations versus the polar coordinates  $(a, \phi)$ , estimated via equation (39). White/black zones indicate over/under dense regions where  $|\Delta\sigma/\sigma|$  exceeds 0.63, while white/black zones in the other greyscale indicate the disk’s latitude  $\beta = z/a$  above/below the invariable plane, with saturation occurring wherever  $|\beta|$  exceeds  $0.86^\circ$ . The online edition of this figure will be linked to an animated sequence of these figures that show the system’s time–evolution.

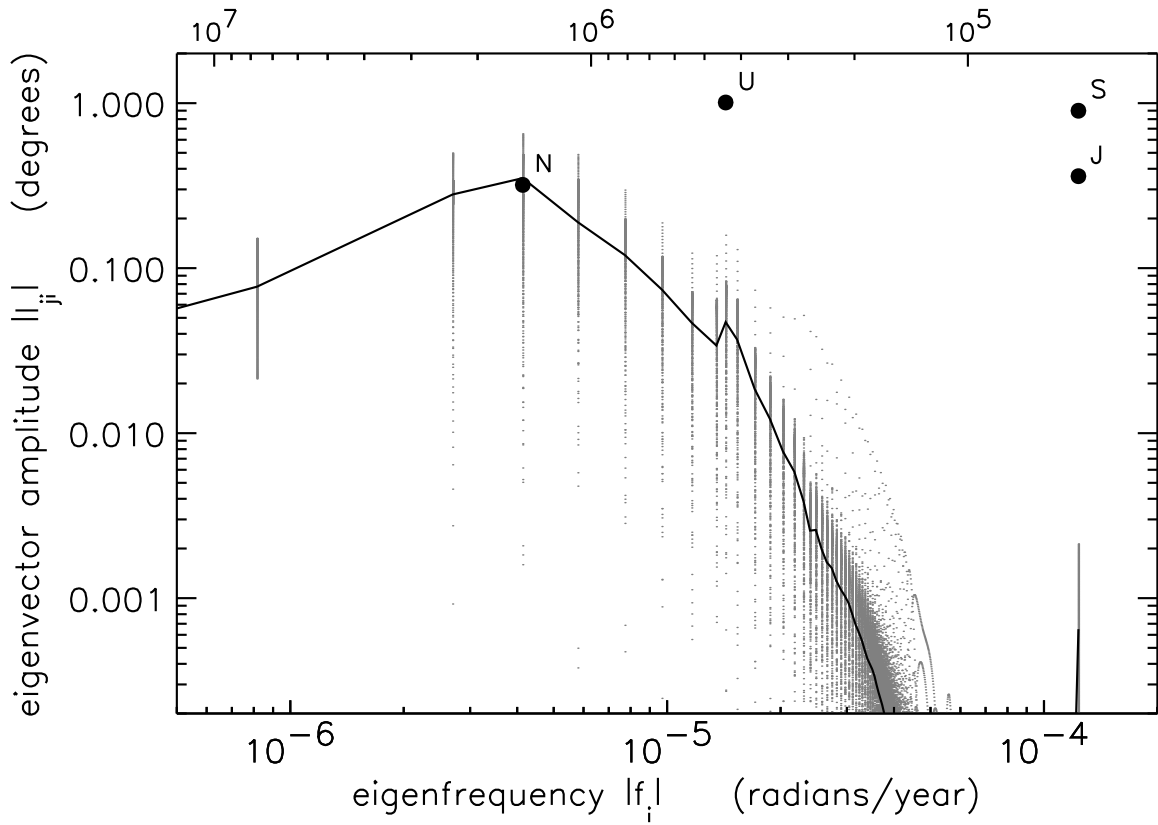
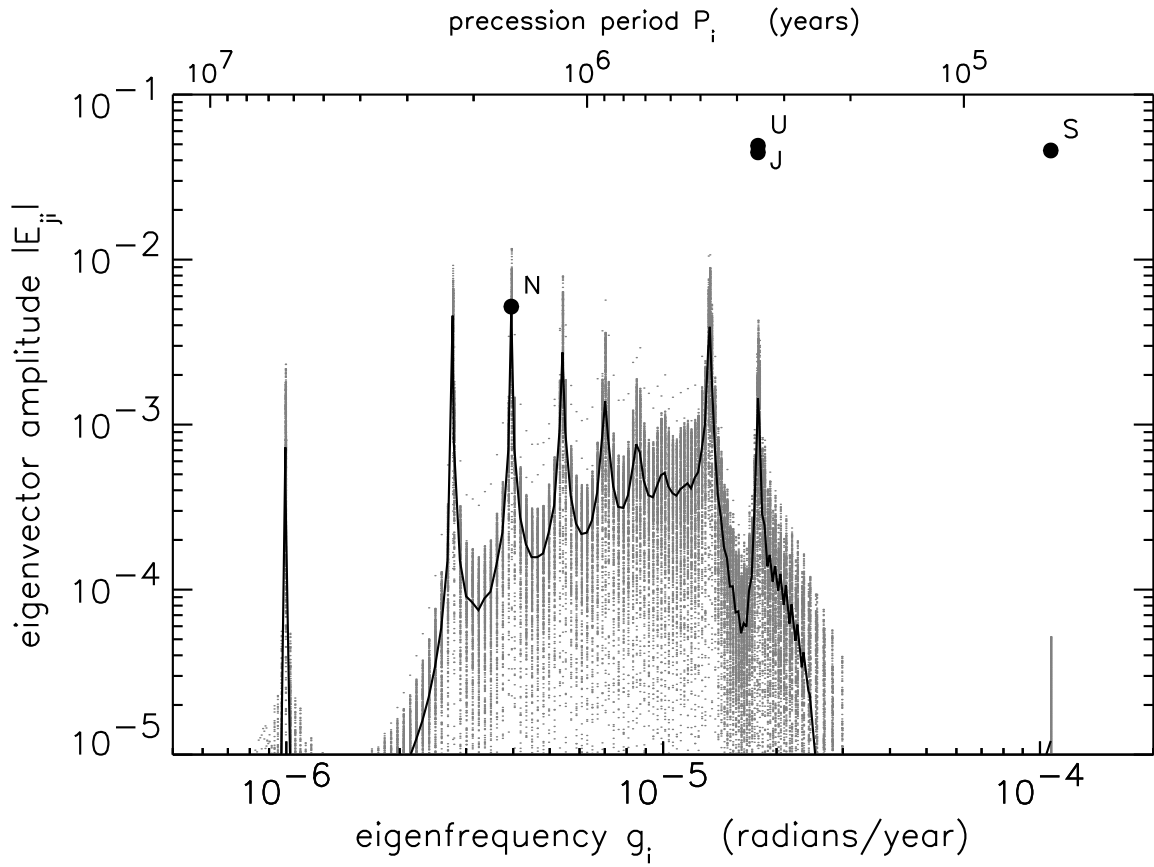


Fig. 3.— The numerous small dots show the individual elements in the disk-rings’ eccentricity eigenvectors  $|E_{ji}|$ , all plotted versus their eigenfrequencies  $g_i$ , as well as the disk-rings inclination eigenvector elements  $|I_{ji}|$  versus  $|f_i|$ , for the system shown in Fig. 2. The solid curves are  $|E_{ji}|$  and  $|I_{ji}|$  averaged over semimajor axes  $45 \leq a_j \leq 55$  AU. The upper horizontal axes are the corresponding precession periods  $2\pi/g_i$  and  $2\pi/|f_i|$ . The large dots indicate the eigenfrequency and eigenvector element that dominates the motion of each giant planet J=Jupiter, S=Saturn, U=Uranus, and N=Neptune.

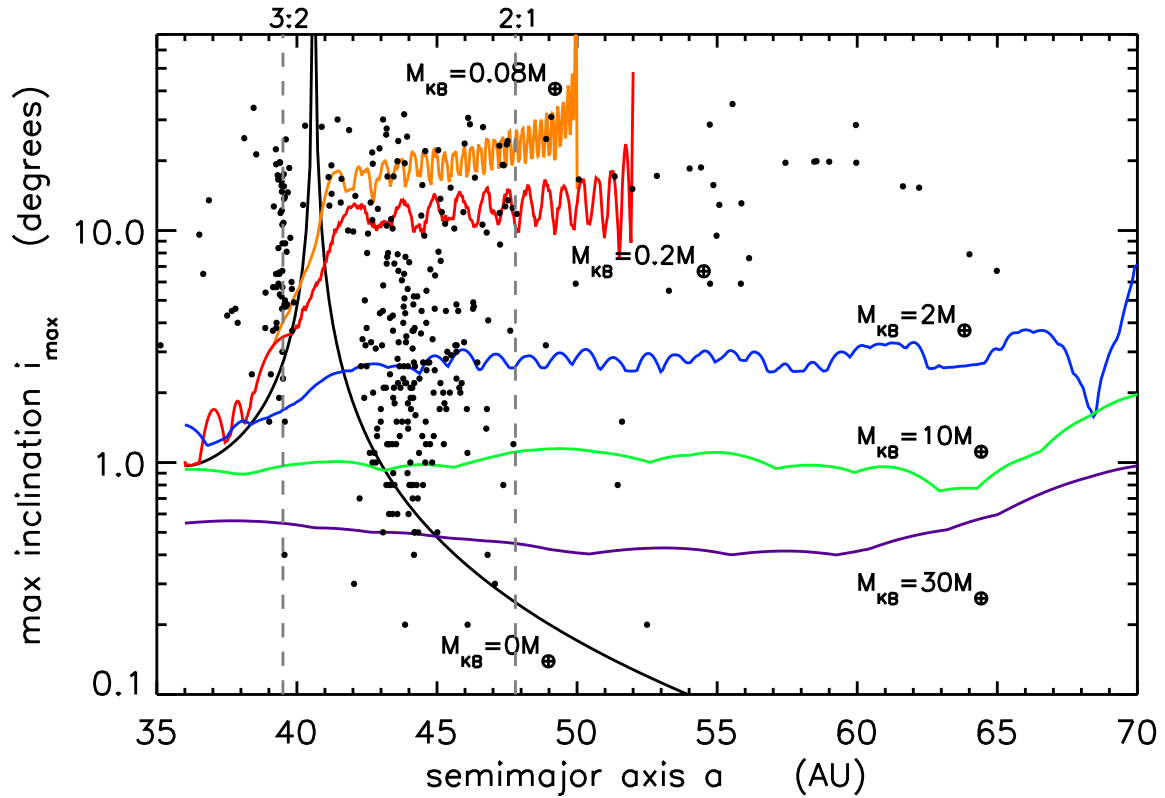
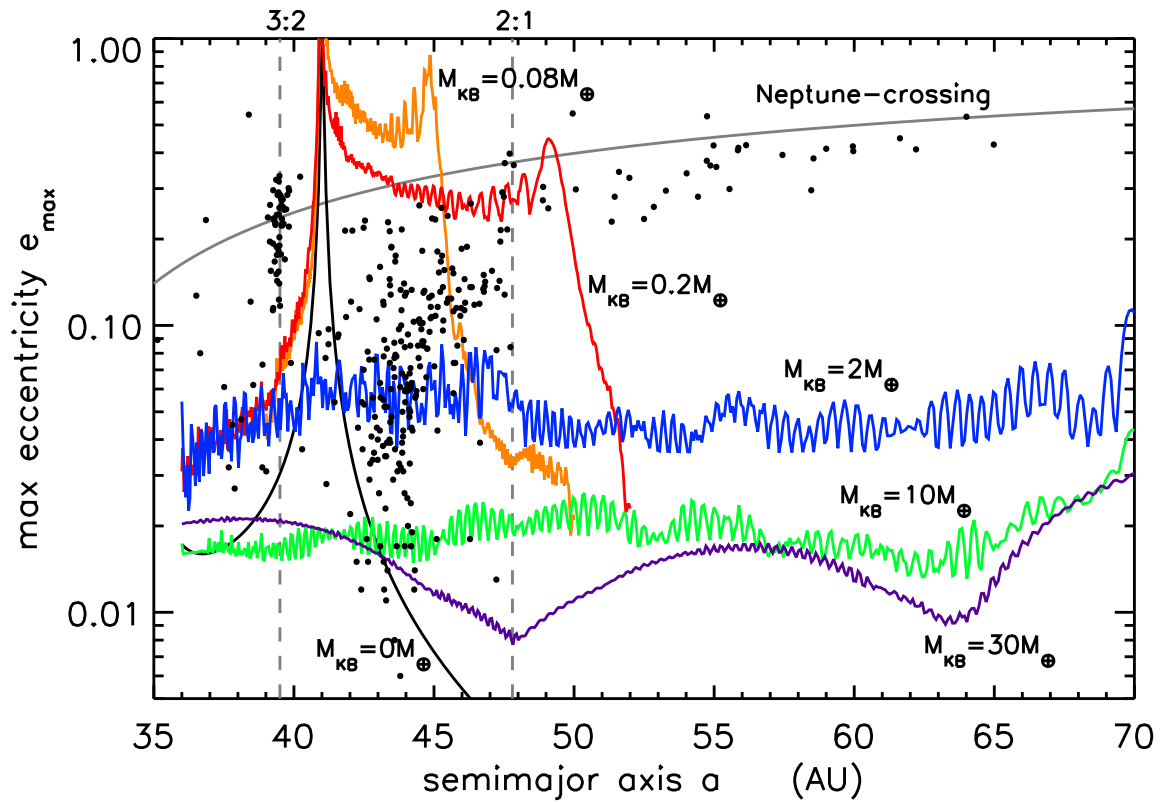




Fig. 4.— The maximum eccentricities  $e_{\max}$  and inclinations  $i_{\max}$  versus semimajor axis  $a$  for simulations having a variety of Kuiper Belt masses  $M_{KB}$ ; see Section 4.2 for model details. Dots indicate the orbits of 340 KBOs observed over multiple oppositions, with orbits provided by the Minor Planet Center. The locations of the 3 : 2 and 2 : 1 resonances are indicated, and orbits above the grey curve are Neptune-crossing.

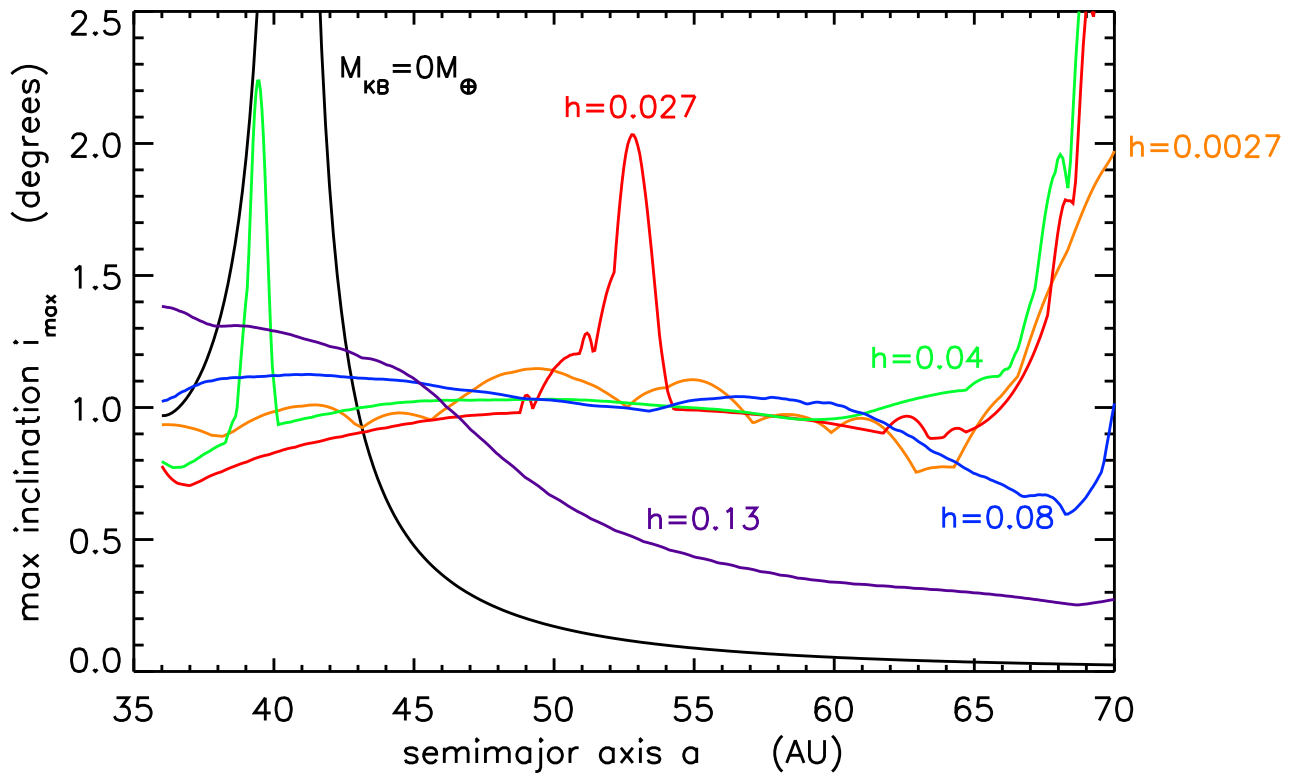
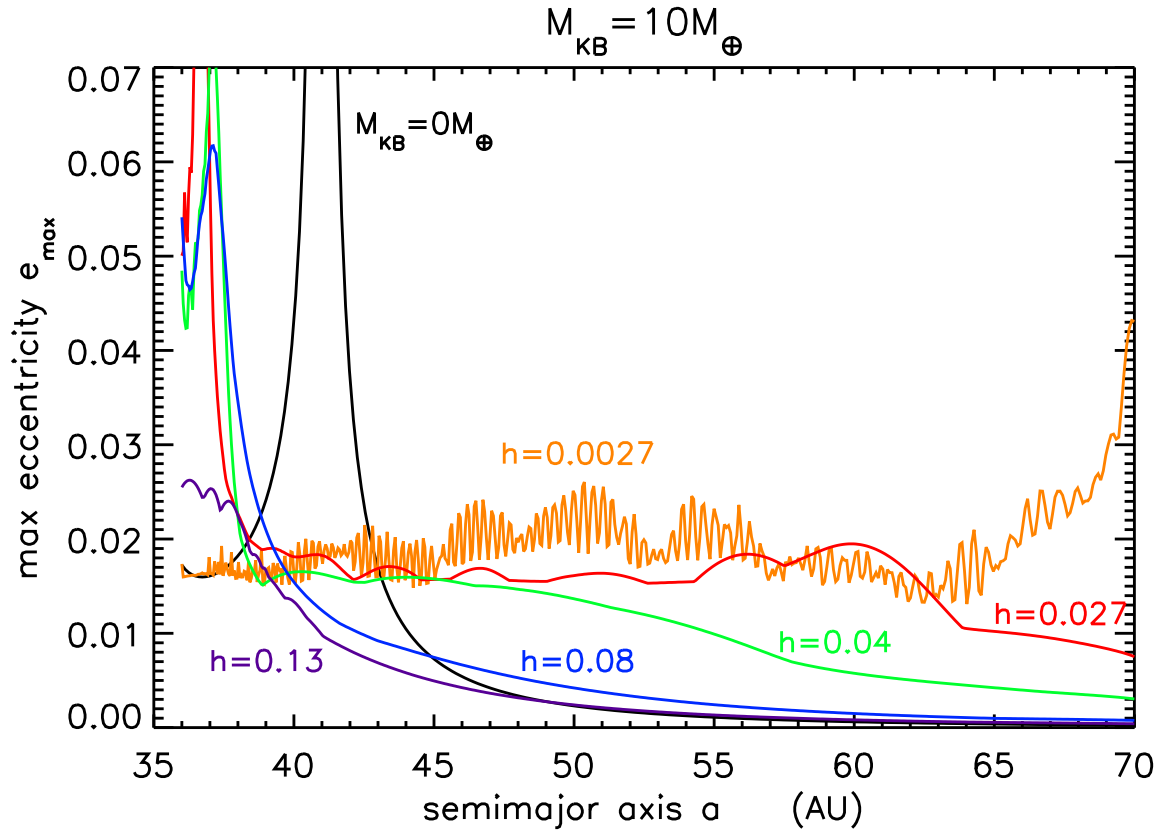


Fig. 5.— Maximum eccentricities and inclinations in a  $M_{KB} = 10 M_{\oplus}$  disk having a fractional thickness  $\mathfrak{h} = 0.0027, 0.027, 0.04, 0.08,$  and  $0.13$ . The black curves are the forced  $e$ 's and  $i$ 's that occur in a massless disk. The characteristic particles size associated corresponding to each disk thickness  $\mathfrak{h}$  may be obtained by setting particle dispersion velocities equal to their surface escape velocity, which corresponds to particle radii of  $R \sim 5000\mathfrak{h}$  km  $\sim 14, 140, 200, 400,$  and  $650$  km, respectively.

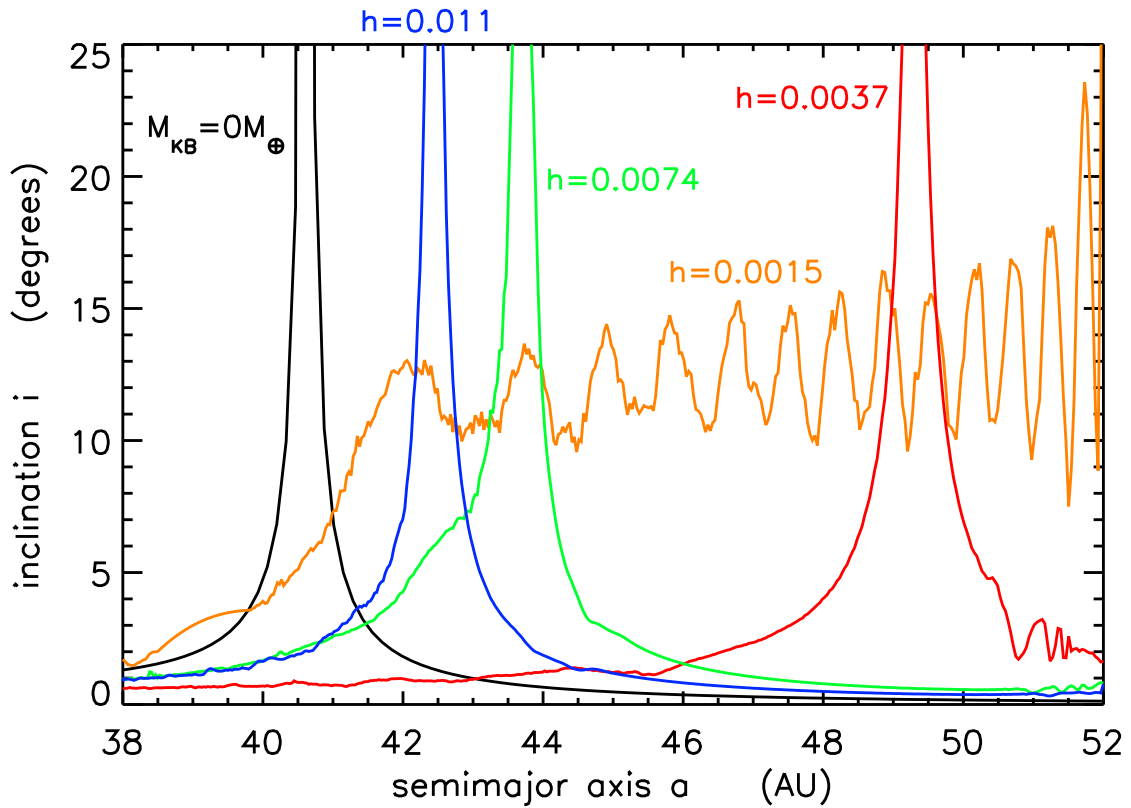
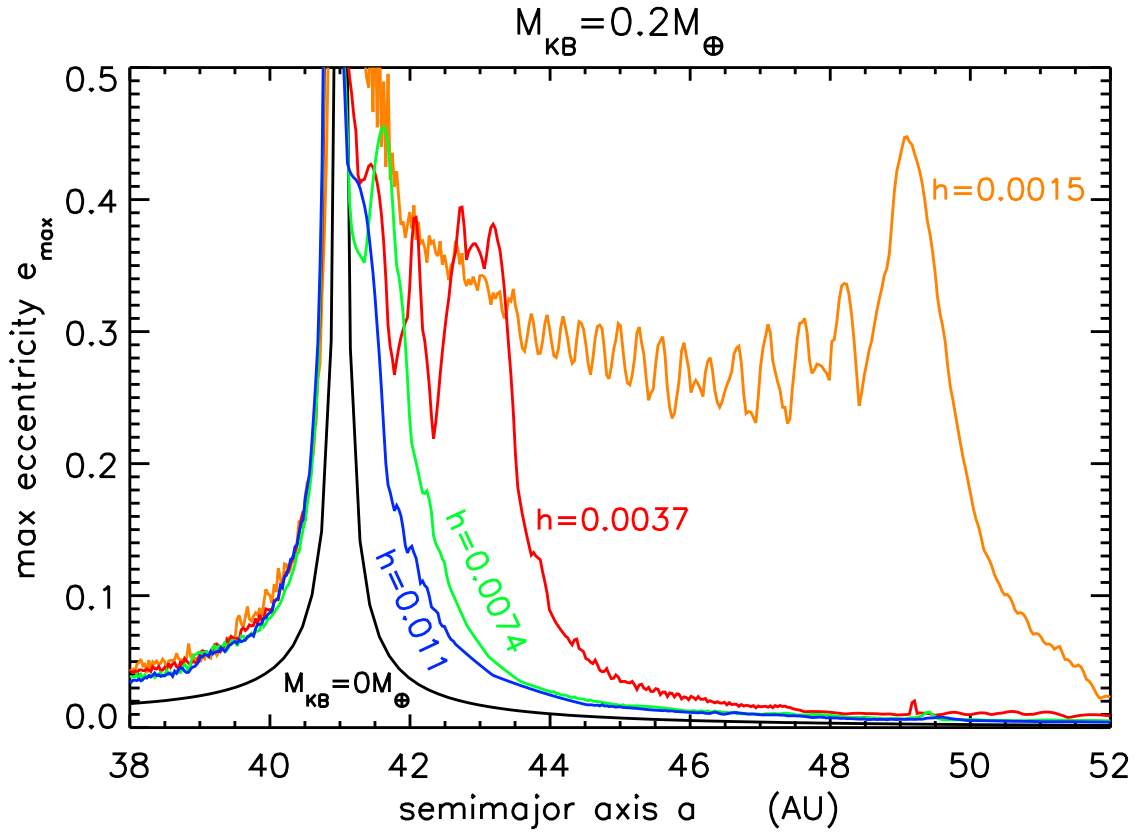


Fig. 6.— The upper plot gives the maximum eccentricities  $e_{\max}$  in a  $M_{KB} = 0.2 M_{\oplus}$  disk having thicknesses  $\mathfrak{h} = 0.0015, 0.0037, 0.0074,$  and  $0.011$ . The lower plot gives the *average* inclinations  $i$  that occur after the bending wave has stalled. The exception is the orange  $\mathfrak{h} = 0.0015$  curve; this wave does not stall, so this curve shows the maximum inclination  $i_{\max}$ . The black curves are the forced  $e$ 's and  $i$ 's that occur in a massless disk.